Multi-objective solid electrolyte design of tetragonal and cubic inverse-perovskites for all-solid-state lithium-ion batteries by high-throughput DFT calculations and AI-driven methods

Randy Jalem[1,*], Yoshitaka Tateyama[1], Kazunori Takada[1], and Seong-Hoon Jang[1]

[1]Center for Green Research on Energy and Environmental Materials (GREEN), National Institute for Materials Science (NIMS), 1-1 Namiki, Tsukuba, Ibaraki 305-0044, Japan

Abstract

Solid electrolytes (SEs) are crucial materials to realize highly safe and practical all-solid-state Li^+ ion batteries. Here, we performed a large-scale computational SE screening on a chemical space of >10,000 Li-rich inverse-perovskite (*ip*) compounds with tetragonal and cubic structures by high-throughput DFT and AI-driven methods. A total of 1,413 novel candidate compounds were predicted to be synthesizable based on thermodynamic decomposition energy (E_d) and machine-learned experimental synthesis likelihood (L_s). These compounds were further screened using a Pareto-front approximation set of a multi-objective Bayesian optimization task for k = 3 DFT-calculated SE properties (f_k, with k = 1, 2, and 3): i) electrochemical window from electronic band gap energy (f_1: E_g), ii) chemical stability by reaction with moisture (f_2: E_h), and iii) 400-K bulk Li^+ ion conductivity (f_3: Λ). As a result, the compound list was reduced down to 24 candidate *ip* SEs, examples include *Cm* $Li_8O_2Cl_3Br$ (E_d = 0, L_s > 0.5, E_g = 4.74 eV, E_h = -33.22 kJ/mol, Λ = 9.0 x 10^{-4} S/cm), *Amm*2 Li_8OSCl_4 (E_d = 0.070 eV/atom, L_s > 0.5, E_g = 4.14 eV, E_h = -40.70 kJ/mol, Λ = 9.2 x 10^{-2} S/cm), and *Cmcm* $Li_{12}O_3SeClBr_3$ (E_d = 0.097 eV/atom, L_s > 0.5, E_g = 3.36 eV, E_h = -86.88 kJ/mol, Λ = 7.8 x 10^{-1} S/cm). Possible solid-state synthesis routes for the screened SE candidates were also explored using thermodynamic phase competition analysis and classical-nucleation-theory reaction barrier. Aside from providing a well-informed list of potentially novel *ip*-type SEs, our work also reports on an effective calculation methodology for tiered large-scale material screening which, at the same time, incorporates 'small data' learning on target property datasets that are computationally expensive to obtain. The generated datasets are expected as well to be of great utility for future data-driven material design efforts.

Introduction

A low-carbon society has been for some time now a major goal of many countries that desire to further elevate the quality of life of people and be more responsive in the protection of the environment by limiting on fossil fuel dependence for energy generation. One specific technology that is expected to play a key role in this area is the all-solid-state rechargeable Li^+ ion battery (ASSB).[1-3] A high-performance ASSB is expected to meet several industry requirements, particularly on energy density, safety, and reliability. It can become widespread in applications such as electric vehicles (EVs), backup power, and household use.[1]

To achieve high energy density, an ASSB with a Li metal anode (3,860 mAh/g in theoretical capacity) is strongly sought and many R&D efforts have since been made so that it can become viable technology-wise.[4] On the other hand, to realize high practical capacity, high-voltage cathodes are needed, one example is a recently designed $LiNi_{0.8}Mn_{0.1}Co_{0.1}O_2$ (NMC811) compound which is capable of 81.3% capacity retention after 2,000 cycles (at 1.5C rate) and a specific energy of up 631.1 Wh/kg.[5] The combination of Li metal anode and high-capacity cathode is expected to meet the driving mileage demand for EVs.[6-7] In addition, another critical component towards unlocking a high-performance ASSB is the solid electrolyte (SE) which has a role of shuttling the charge carrier (Li^+) ions between the anode and the cathode, and vice versa, during battery discharge/charge operations. Several SE design goals include: i) Li-superionic conductivity, ii) mechanical robustness in a sufficiently thin configuration, iii) chemical stability during battery work operation, and iv) (electro)chemical compatibility with other solid-state cell components.[8-11] So far, a number of promising SEs were reported to satisfy the ionic conductivity requirement (i.e., 10^{-3} S/cm or better), but finding a material that also meets other sought properties at the same time has still remained a longstanding challenge.[10,12-15]

To speed up the search of novel SEs, high-throughput density functional theory calculations (HT-DFT) and methods based on artificial intelligence (AI) have been employed recently in combination to provide experimentalists with a list of candidate materials that should be highly prioritized for actual synthesis and characterization. Several examples work on computational SE material screening have been reported, but they only focus on a single or a few SE properties at a time. Examples of these properties are ionic conductivity, thermodynamic stability, (electro)chemical stability, and suppression ability vs. Li dendrite growth.[16-22]

Among the class of already reported SEs, Li-rich inverse-perovskite (*ip*) compounds show great promise in terms of ionic conductivity and electrochemical property.[23-25] These compounds can also demonstrate mechanical softness to enable for an intimate contact with electrodes and other battery materials in the cell for reduced interfacial resistance, show exceptional stability against Li metal via formation of electronic-insulating but ionic-conducting decomposition interphase layer, and be rapidly synthesized with high scalability[26-27] Their general formula can be expressed as $Li_{3n+1}X_nZ_{n+1}$ which, by symmetry, can be characterized as tetragonal (*t-ip*) for n $\in$ [1, 2, 3, …] and cubic (*c-ip*) for n = ∞ (i.e., Li_3XZ as reduced formula); the value of n is indicative of the thickness of the X/Z-Li (anion-centered) 2D slabs that are stacked in the crystallographic long-axis direction.[28] Given the long development history of normal perovskites, it naturally follows that there is also a wide variety of structure derivatives (i.e., based on index n) and configurations (i.e., site alloying + symmetry group-subgroup relations) for *c-ip* and *t-ip* compounds. Consequently, there is a large chemical search space that is yet to be explored for undiscovered novel compounds. We have partly demonstrated this in our recent work which reported on several DFT-predicted novel *t-ip* (n = 1) SE candidates on a chemical space containing about 500 compounds.[29]

Here, using a combination of HT-DFT calculations and AI-driven methods, we explored the chemical space of >10,000 *in-silico t-ip* and *c-ip* compounds to find promising novel SEs. Multiple DFT-calculated SE properties were used as screening criteria: thermodynamic stability (by convex hull method), electrochemical window upper bound based by electronic band gap energy, air-exposed chemical stability by thermodynamic bulk reaction energy vs. H_2O, and bulk Li^+ ionic conductivity from multiple-temperature ab initio molecular dynamics (AIMD) approach. Additionally, the *in-silico* compounds were evaluated for their synthesizability and possible rational synthesis routes by DFT and recent state-of-the-art machine learning techniques. Aside from the useful atomistic-level insights on SE properties as well as practical information on *ip* compound synthesis, this study also provides a useful methodology template for multi-objective material SE design (i.e., Pareto-based optimization) and a large-scale DFT dataset of potentially novel compounds that can be exploited for future data-driven material design studies.

Computational details

Structure geometry optimization

DFT calculations were performed using the VASP software[30,31] which is based on the projector augmented wave (PAW) approach[32-34]. The electron exchange-correlation part of the Hamiltonian was described using the generalized gradient approximation (GGA) method by Perdew, Burke, and Ernzerhof (PBE).[35,36] Three parent crystal structure aristotypes based on the *ip* block stacking were used for chemical space generation: Li_4XZ_2 (n = 1), $Li_7X_2Z_3$ (n = 2) and Li_3XZ (n = ∞); the atomic coordinate data were taken from the Inorganic Crystal Structure Database (ICSD),[37] see Figure 1. Except for the Li pseudopotential which explicitly includes the semi-core s states as valence states, standard pseudopotentials were employed for H, X (O, S, Se, Te) and Z (F, Cl, Br, I) elements. A 520-eV kinetic cutoff energy was set with a k-points resolution of ≥ 1000 in a Monkhorst-Pack grid scheme.[38] All calculations were carried out with spin polarization. Energy and residual forces were ensured to be less than 1 meV/atom and 0.01 eV/Å, respectively.

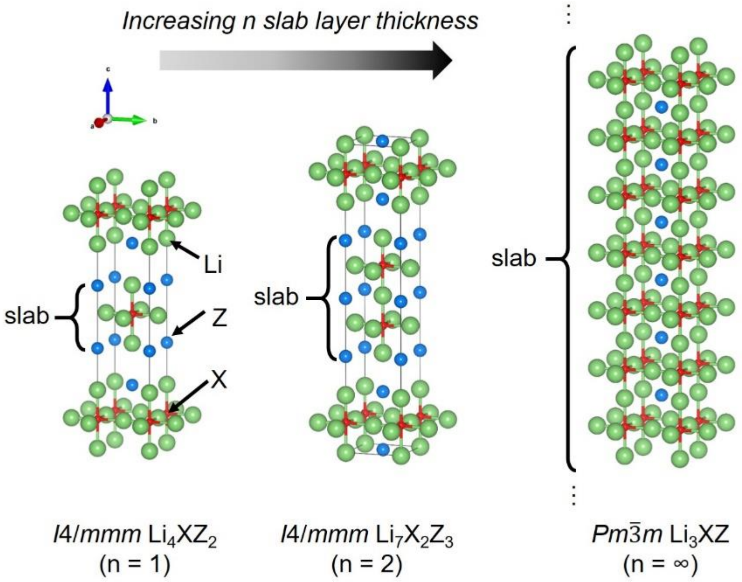

Figure 1. Schematic illustration of different inverse perovskite $Li_{3n+1}X_nZ_{n+1}$ crystal structures classified according to the slab layer thickness expressed as integer n > 0 relative to the XLi_6 unit along *c*-direction, such as in the case of *I*4/*mmm* tetragonal symmetry (e.g., n = 1, n = 2). As the XLi_6 slab layer becomes infinitely thick (i.e., n = ∞), the structure assumes the $Pm\bar{3}m$ cubic symmetry. Green, red, blue spheres represent Li^+ cation, X^{2-} anion, and Z^- halide anion, respectively.

Thermodynamic phase stability evaluation

In-silico t-ip and *c-ip* compounds were evaluated for their thermodynamic stability by DFT decomposition energy (E_d) calculation.[39] Briefly, a convex hull of tie lines formed by ground-state phases was constructed. In this formulation, ground-state phases lie on the hull surface as vertices and, by definition, have a hull distance of zero (i.e., E_d = 0). Any *in-silico* compounds that lie above the hull surface of ground-state phases are predicted as metastable or as compounds that are thermodynamically driven to decompose. Formally, E_d (in eV/atom) was calculated according to the following equation:

$$E_d = \Delta H_f - \Delta H_c, \qquad (1)$$

where ΔH_f and ΔH_c are the convex hull energies (using formation enthalpies, pressure and entropy effects were considered negligible at ambient conditions), relative to the phase equilibria at composition c (i.e., related to stable competing phases). Calculations were performed using the total energies of relevant DFT-calculated ICSD compounds and compounds from the Materials Project database, using the latter's application programming interface (i.e., Pymatgen library).[40,41]

Multi-objective optimization of electrolyte properties

Three DFT-calculated SE-related properties were used as objective functions (f_k, where $k \in \{1,2,3\}$) for finding optimal SE candidates. These are as follows: i) electrochemical window upper bound based on electronic band gap energy (f_1: E_g), ii) chemical stability measure based on hydration energy (f_2: E_h), and iii) bulk Li^+ ionic conductivity at 400 K (f_3: Λ).

Previous works have already used E_g as a filter for SE electrochemical stability window,[42] following the general observation that a large E_g often correlates with high electrochemical stability and negligible electronic conductivity. The value of E_g was estimated from the energy difference between the valence band maximum (VBM) and conduction band minimum (CBM) of a compound's DFT-PBE electronic density of states.

For E_h, the Li^+/H^+ exchange process leading to LiOH formation was considered as the relevant reaction for chemical stability evaluation in air:[43-44]

$$Li_aX_bZ_c + H_2O \rightarrow Li_{a-1}HX_bZ_c + LiOH, \qquad (2)$$

where $Li_aX_bZ_c$ is the *ip* compound (e.g., $\{a,b,c\} = \{81,27,27\}$ for $Li_{81}X_{27}Z_{27}$ supercell). A supercell size of at least10 Å in cell edge lengths was imposed to remove any unphysical interaction between the atoms in the main cell and those from the mirror-image cells due to periodic boundary condition. For the Li-H arrangements, 10 random configurations were generated and then geometry-optimized by DFT. Using the lowest total-energy structure, the reaction free energy with H_2O ($\Delta G_{reaction,H_2O}$) was determined as follows:

$$\Delta G_{reaction,H_2O} = \Delta H - T\Delta S \ (T = 298 \text{ K}), \qquad (3)$$

where $\Delta G_{reaction,H_2O} < 0$ (in kJ/mol) when the reaction is exothermic (i.e., spontaneous reaction with H_2O). Otherwise, the reaction is endothermic ($\Delta G_{reaction,H_2O} > 0$) and would require external energy/heat source to drive the protonation process. A compound with f_2: $E_h > 0$ is thus desired from the viewpoint of SE chemical stability. The entropic term ($T\Delta S$) was computed following the scheme implemented for the Materials Project database and with the pymatgen library.[45] Specifically, the entropy contribution term is added to the DFT energy of any compounds that are liquid or gaseous at room temperature (298 K), such as H_2O in the present work; the entropy data that was used was derived from an experimental dataset source.[46]

For f_3: Λ, AIMD calculation was performed for two types of defect-driven ion transport processes: Li dumbbell (interstitial) and vacancy-driven mechanism.[47] The MD step size was fixed to 1 fs and the target temperature was set to 400 K. For the estimation of bulk Li^+ ion activation energy (E_a), the Arrhenius slope was determined from diffusivity data at several MD temperatures (700, 800, 900, 1000, and 1200 K). In the initial stage of the MD run, structures were equilibrated at the target temperature under NPT ensemble condition for 10 ps.[48] This step was then followed by the actual production run under the NVT ensemble condition for 50 ps.[49] The time-averaged mean square displacement (MSD) of Li^+ ions (in Å^2) was calculated by the following equation:[50]

$$MSD = \langle[\boldsymbol{r}(t+\tau) - \boldsymbol{r}(t)]^2\rangle, \qquad (4)$$

where $\boldsymbol{r}(t)$ is the position Li at time t, and τ is the lag time between positions. The diffusion coefficient (cm^2/s) was estimated based on the Einstein-Smoluchowski equation:[51]

$$D = \lim_{t\to\infty}[(1/2dt)\langle[\boldsymbol{r}(t+\tau) - \boldsymbol{r}(t)]^2\rangle], \qquad (5)$$

where d is the dimensionality of the lattice for Li^+ ion diffusion. It was previously determined that *t-ip* and *c-ip* compounds have d = 2 and d = 3, respectively. It is noteworthy to mention that D was derived from the slope at the diffusive regime of the MSD plot; additional details are provided in the Supporting Information section (see Fig. S1). The Nernst-Einstein equation was then used to calculate the AIMD ionic conductivity (Λ):[52]

$$\Lambda = \rho F_c^2 z_c^2 D/RT, \qquad (6)$$

where ρ is the mass density of Li^+ ions, z_c is the charge of Li^+ ion, F_c is the Faraday constant, R is the gas constant, and T is the temperature.

Machine learning methods

Machine-learning descriptors of a given compound i ($\boldsymbol{x}_i$) were extracted from its chemical and structure-/geometric-based information. Three natural descriptor groupings were considered: atom electronegativity (EN), atom-centered Voronoi real-feature values (VR), and atom-atom partial radial distribution functions (PF). Features were encoded by binning approach, essentially converting the compound information into histogram vectors.[53]

A surrogate-assisted multi-objective optimization algorithm based on Bayesian optimization (MOBO) with a batch-compound sampling scheme was employed, see Algorithm 1.[54] The MOBO goal here was to iteratively improve a Pareto-front approximation set of SE-property objective functions. The non-dominated points of the Pareto front are referred to as the optimal solution sets (i.e., best *ip* compounds). Without loss of generality, objective functions $y^{(k)}$ (i.e., k = 3, $\{y^{(1)}$: f_1, $y^{(2)}$: f_2, $y^{(3)}$: $f_3\}$) were treated as mutually independent from each other. The y function was approximated by a Gaussian process (GP) model that is characterized by a mean function $m(\boldsymbol{x})\colon \boldsymbol{X} \to \mathbb{R}$ and a kernel (or covariance) function: $\boldsymbol{X} \times \boldsymbol{X} \to \mathbb{R}$. The y values ($y_{1:n} \coloneqq [y(\boldsymbol{x}_1), \dots, y(\boldsymbol{x}_n)]^\top$) are assumed to be drawn from a distribution with a Gaussian nature at arbitrary finite n data points $\boldsymbol{x}_{1:n}$:[55]

$$y_{1:n} | \boldsymbol{x}_{1:n} \sim \mathcal{N}(m_{1:n}, \boldsymbol{K}), \qquad (7)$$

where $K_{i,j} = k(\boldsymbol{x}_i, \boldsymbol{x}_j)$ $(i, j \in \{1, \dots, n\})$. The base functional form of $k(\boldsymbol{x}_i, \boldsymbol{x}_j)$ was formulated with a radial basis function:

$$k(\boldsymbol{x}_i, \boldsymbol{x}_j) = \sigma_f^2 \exp\left(-\left\|\boldsymbol{x}_i - \boldsymbol{x}_j\right\|^2 / 2l^2\right), \qquad (8)$$

where σ_f^2 is for the positive-valued signal variance (kernel amplitude), $\left\|\boldsymbol{x}_i - \boldsymbol{x}_j\right\|^2$ is for the squared Euclidean distance between two sample compounds (represented as descriptor vectors), and l is for the positive-valued lengthscale. The variation of two hyperparameters, σ_f^2 and l, results in the variation in the *a priori* correlation between sample compounds and consequently, the prediction variability for y. The latter is also assumed to have an associated noise (ϵ):

$$y_i = f(\boldsymbol{x}_i) + \epsilon_i \qquad (9)$$

with $\epsilon_i \sim \mathcal{N}(0, \sigma_{noise}^2)$. Given n training samples $\mathcal{D}_t \coloneqq \{\boldsymbol{x}_i, y_i\}_{i=1}^{t}$, a posterior for f_k: $f(\boldsymbol{x})$ can be expressed into the following:

$$f(\boldsymbol{x}) | y_{1:t} \sim \mathcal{N}(\mu_t(\boldsymbol{x}), \sigma_t^2(\boldsymbol{x})), \qquad (10)$$

$$\mu_t(\boldsymbol{x}) = m(\boldsymbol{x}) + \boldsymbol{k}(\boldsymbol{x})^\top \left(\boldsymbol{K} + \sigma_{noise}^2 \boldsymbol{I}\right)^{-1} (y_{1:t} - m_{1:t}), \qquad (11)$$

$$\sigma_t^2(\boldsymbol{x}) = k(\boldsymbol{x}, \boldsymbol{x}) - \boldsymbol{k}(\boldsymbol{x})^\top \left(\boldsymbol{K} + \sigma_{noise}^2 \boldsymbol{I}\right)^{-1} \boldsymbol{k}(\boldsymbol{x}), \qquad (12)$$

where $\boldsymbol{k}(\boldsymbol{x})$, $m_{1:t}$, $\mu_t(\boldsymbol{x})$, and $\sigma_t^2(\boldsymbol{x})$ represents the covariance among $\boldsymbol{x}$ and $\boldsymbol{x}_{1:t}$, the mean function of $\boldsymbol{x}_{1:t}$, the posterior mean, and the posterior variance, respectively. The GP models were improved by tuning the hyperparameters by marginal likelihood maximization approach.[56]

To avoid convergence issues related to the high-dimensionality of $f(\boldsymbol{x})$, a descriptor reduction step was performed as follows:[57,58] i) projecting each of the grouped descriptor vectors (EN, VR, PF) down to 30 latent variables by kernel PCA,[59] and ii) decomposing $f(\boldsymbol{x})$ into a linear combination relative to the descriptor groups:

$$f(\boldsymbol{x}) = \textstyle\sum_{F=1}^{F=6} f(\boldsymbol{x}_i) + \boldsymbol{\epsilon}, \qquad (13)$$

where $F = 6$ denotes 6 decomposition terms for $f(\boldsymbol{x})$ and $\boldsymbol{\epsilon} \sim \mathcal{N}(0, \sigma_\epsilon^2)$ is the imposed residual that is a zero-mean Gaussian noise. Moreover, each $f(\boldsymbol{x}_i)$ was formulated with sub-kernels k_F as follows:

$$k_1 = k(\boldsymbol{x}, \boldsymbol{x}')_{EN}, \qquad (14)$$

$$k_2 = k(\boldsymbol{x}, \boldsymbol{x}')_{VR}, \qquad (15)$$

$$k_3 = k(\boldsymbol{x}, \boldsymbol{x}')_{PF}, \qquad (16)$$

$$k_4 = k(\boldsymbol{x}, \boldsymbol{x}')_{EN} k(x, x')_{VR}, \qquad (17)$$

$$k_5 = k(\boldsymbol{x}, \boldsymbol{x}')_{EN} k(x, x')_{PF}, \qquad (18)$$

$$k_6 = k(\boldsymbol{x},\boldsymbol{x}')_{VR}\, k(x,x')_{PF}, \tag{19}$$

where k_1, k_2, and k_3 are sub-kernels for the original (primary) descriptor groups (EN, VR, PF) while k_4, k_5, and k_6 are secondary product sub-kernels derived from k_1, k_2, and k_3. The abovementioned algorithm and the machine-learning models were coded using the python libraries scikit-learn and GPy.[60,61]

At each MOBO iteration step, a batch of query compounds were selected by an infill criterion based on hypervolume improvement with upper confidence bound ($uHVI$):[54]

$$uHVI = V_1 - V_0 = V\left(\boldsymbol{y}(d_0) \cup g\left(\boldsymbol{x}_{t+1,m}\right)\right) - V\left(\boldsymbol{y}(d_0)\right), \tag{20}$$

where $g\left(\boldsymbol{x}_{t+1,m}\right) = \mu_{t+1.m}(\boldsymbol{x}) + \sigma_{t+1.m}(\boldsymbol{x})$ is the upper confidence bound of a sample compound m related to the DFT-calculated (f_1, f_2, f_3) values. Each sample compound m in the list of M unevaluated candidates ($m \in M$) was added to d_0 at a time. All the $uHVI$ scores of M candidates were then sorted in decreasing order, with the top z = 10 compounds in the ordered list being picked by a greedy selection rule. This batch of selected compounds were subsequently evaluated for their (f_1, f_2, f_3) values by DFT. The sequential nature of MOBO sampling makes it highly suitable for 'small data' learning on target properties that are expensive to obtain, such in the case of AIMD ionic conductivity.[58]

Since the optimal direction of the present MOBO sampling strategy was formulated towards large positive values of f_1, f_2, and f_3, the overall optimization setting can then be regarded as a maximization problem. Additionally, (f_1, f_2, f_3) values were weighted equally with the following scaling transformation:

$$f_1 \rightarrow -f_1, \tag{21}$$

$$f_2 \rightarrow -f_2/100, \text{ and} \tag{22}$$

$$f_3 \rightarrow -10f_3. \tag{23}$$

The negative signs were applied for convenience in the hypervolume calculation step for the $uHVI$ score. The nadir point was fixed to a scaled coordinate of (0, -10, 0) which was determined as the physically meaningful bound for (f_1, f_2, f_3). The batch compound sampling procedure was terminated when all the best (f_1, f_2, f_3) values do not change anymore for at least 3 MOBO iteration steps. The numerical calculation of hypervolume was performed using the python package PyGMO.[62] Table 1 shows the MOBO algorithm in detail.

Table 1. Algorithm description of the compound sampling workflow that was developed in this work which is based on multi-objective Bayesian optimization (MOBO) with upper confidence bound (UCB) and greedy-selection batch sampling (k = 3 objective functions)

```
1. Build initial dataset $d_0 = (\boldsymbol{x}_t, (y_t^1, y_t^2, y_t^3))$.
2. Calculate initial hypervolume $V_0 = V(d_0)$.
```

```
3. Build $GP$ models for $k$ objective functions using $d_0$.
4. Use $GP$ models to estimate $\left(g^{(1)}_{t+1,m}(\boldsymbol{x}), g^{(2)}_{t+1,m}(\boldsymbol{x}), g^{(3)}_{t+1,m}(\boldsymbol{x})\right)$ of all sampling point $m$ in the list of unevaluated M samples (i.e., $g_{t+1,m}(\boldsymbol{x}) = \mu_{t+1,m}(\boldsymbol{x}) + \sigma_{t+1,m}(\boldsymbol{x})$).
5. For each $m$ unevaluated point $(x_{t+1})$, calculate separately for hypervolume $V_1 \leftarrow V(\boldsymbol{y}(d_0) \cup g_{t+1,m}(\boldsymbol{x}))$ and expected hypervolume improvement with UCB $(uHVI = V_1 - V_0)$.
6. Select top $z$ candidates based on $argmax(uHVI)$ from $\boldsymbol{x}_{t+1,m}$ samples.
7. Evaluate $\boldsymbol{y}$ of top $z$ candidates (z < M) by DFT calculations.
   $d_1 = \{(\boldsymbol{x}_{t+1,1}, (y^1_{t+1,1}, y^2_{t+1,1}, y^3_{t+1,1})), (\boldsymbol{x}_{t+1,2}, (y^1_{t+1,2}, y^2_{t+1,2}, y^3_{t+1,2})),$
   $(\boldsymbol{x}_{t+1,3}, (y^1_{t+1,3}, y^2_{t+1,3}, y^3_{t+1,3})), \ldots, (\boldsymbol{x}_{t+1,z}, (y^1_{t+1,z}, y^2_{t+1,z}, y^3_{t+1,z})).$
8. Stopping criterion met?
   Yes: Output Pareto-front approximation set
   No: Perform update ($d_0 \leftarrow d_0 \cup d_1$, $V_0 \leftarrow V_0 \cup V_1$), repeat steps 3-7.
```

Fig. 2 shows the schematic workflow of the MOBO-based SE screening task. In step 1, derivative structures and series compounds from parent lattices (*I*4/*mmm* for n > 1, $Pm\bar{3}m$ for n = ∞) were generated by: i) supercell operation with up to a maximal Miller index of 3 and ii) exclusive anion-site isovalent substitution with symmetry ordering constrained by maximal group-subgroup relations[63]. The sub-concentration ratios of the alloying elements at the X (O, S, Se, Te) and Z (F, Cl, Br, I) sites were restricted to 1:0, 0.75:0.25, 0.5:0.5, 0.67:0.33, and vice versa. Using heuristic guidelines on metastability,[64,65] the different anionic configuration (microstates) in a given composition were each treated as distinct compounds that potentially can be accessible during actual experimental synthesis. As a result, the generated initial chemical space contains multiple entries at each unique composition. In step 2, the initial chemical space was reduced using a phase stability filter of E_d < 0.1 eV/atom.[65] The reduced chemical space was then used for the proposed MOBO-based SE screening task in step 3, with batch compound sampling in an iterative manner that involves the explicit DFT calculations of f_1: E_g, f_2: E_h, and f_3: Λ. In step 4, the non-dominated points (i.e., optimal compounds) were determined from the constructed the Pareto-front approximation set (i.e., SE-property frontier surface).

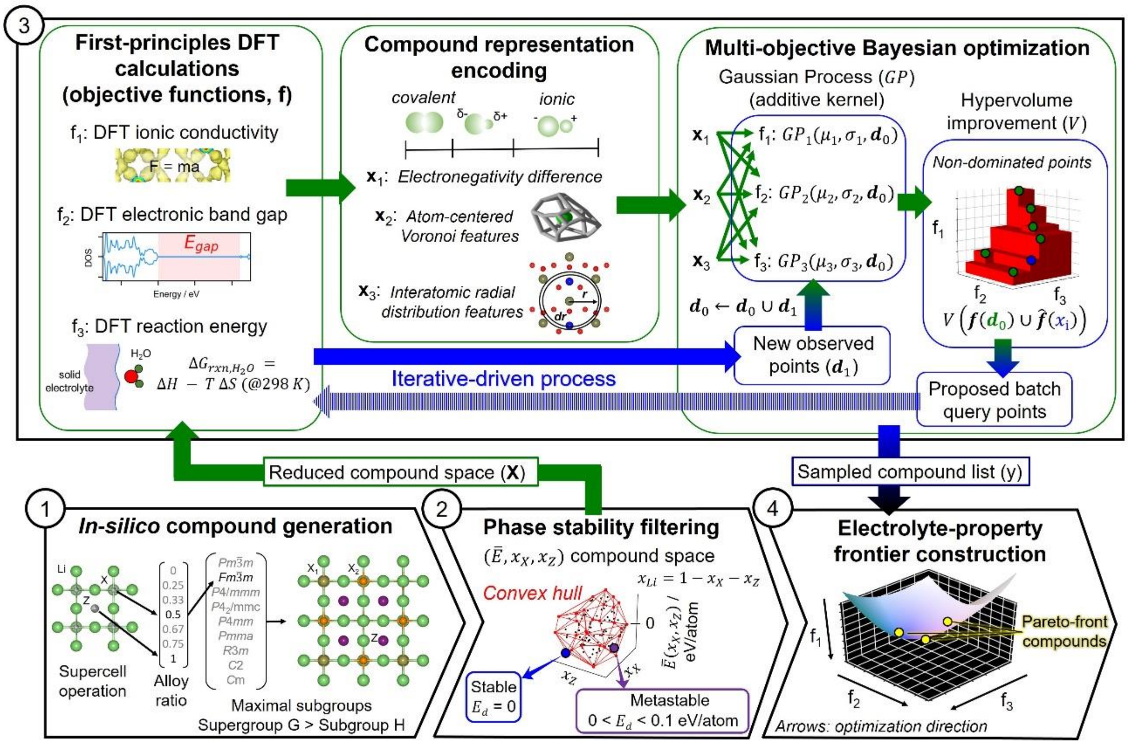

Figure 2. Schematic workflow of the multi-objective Bayesian-optimization compound sampling that was employed in this work: (1) *in-silico* compound generation by anion site alloying and symmetry constraints, (2) thermodynamic (meta)stability filtering by convex hull method for compound space reduction, (3) compound sampling by multi-objective Bayesian optimization (see Table 1 for the algorithm in detail) based on DFT-calculated electrolyte-related properties (f_1: DFT electronic band gap energy in eV, f_2: DFT hydration energy in kJ/mol, f_3: DFT 400-K Li$^+$ ionic conductivity in S/cm), and (4) Pareto-based analysis for the selection of optimal compounds.

Results and discussion

Structure and thermodynamic stability

We previously proposed a modified formulation of the Goldschmidt tolerance factor ($t_{G,ip}$) for *t-ip* compounds, the equation is given by:[29,66]

$$t_{G,ip} = \frac{r_{Li} + \sum_{i=1}^{2} w_{Z,i} r_{Z,i}}{\sqrt{2}\left(\sum_{i=1}^{2} w_{X,i} r_{X,i} + \sum_{i=1}^{2} w_{Z,i} r_{Z,i}\right)}, \qquad (24)$$

where r_{Li}, $r_{X,i}$, and $r_{Z,i}$ are the Shannon ionic radii of Li^+, X^{2-} anion, and Z^-, respectively, with their site-occupancy weights (i.e., 1 for Li^+, $w_{X,i}$ for X^{2-}, and $w_{Z,i}$ for Z^-). Here, we apply equation (24) to also evaluate the structure stability of c-*ip* compounds. Fig. 3a shows the plot on E_d vs. $t_{G,ip}$ of 10,173 *in-silico t-ip* and *c-ip* compounds, highlighting a negative correlation and an increasingly narrower E_d range as $t_{G,ip}$ increases. The physical meaning of $t_{G,ip}$ can be further analyzed with respect to chemistry, as displayed in Fig. 3b which is the E_d heatmap as a function of weighted anion radii at the X and Z sites (see equation 24 denominator). There is a clear underlying structure of positive and negative correlations between E_d and $\sum_{i=1}^{2} w_{X,i} r_{X,i}$ and $\sum_{i=1}^{2} w_{Z,i} r_{Z,i}$, respectively, hinted by an overall shape characterized by low-lying E_d contour lines in the upper left corner and high-lying contour lines in the lower right corner of the energy-stability surface. Consistent with our previous result,[29] *ip* compounds tend to become less stable with less electronegative X anion (i.e., generally larger X anion radius) and/or more electronegative the Z halide anion (i.e., smaller Z anion radius), and vice versa. Given this strong correlation, $t_{G,ip}$ can thus be employed as a general stability screening parameter that encompasses both *t-ip* and *c-ip* compounds.[29,67]

By E_d criterion, 1,501 compounds are predicted to be (meta)stable. Some of these compounds have already been experimentally confirmed previously, thus providing a quantitative validation of our calculation results: Li_3OCl (0 eV/atom), Li_3OBr (0.017 eV/atom), $Li_3OCl_{0.5}Br_{0.5}$ (0.007 eV/atom), $Li_7O_2Br_3$ (0.006 eV/atom), and Li_6OSI_2 (0.052 eV/atom). Meanwhile, several unreported and potentially novel compounds are predicted as stable or ground-state phases (i.e., DFT-E_d = 0), they belong to O- and Br/Cl-bearing compositions: *I*4/*mmm* $Li_7O_2Cl_3$ (*I*4/*mmm*), $Li_7O_2ClBr_2$ (*I*4*mm*, *P*4/*mmm*, *P*4/*nmm*), $Li_8O_2ClBr_3$ (*P*4/*nmm*, *P*4/*mmm*, *P*4*mm*, *Pmm*2, *P*$\bar{4}$*m*2, *Cm*, *P*1), Li_4OClBr (*P*4*mm*, *P*4/*mmm*, *I*4*mm*, *P*4*mm*, *Pmm*2, *Pma*2, *Cm*), $Li_8O_2Cl_3Br$ (*P*4/*mmm*, *P*4/*nmm*, *P*4*mm*, *P*$\bar{4}$*m*2, *Pmm*2, *Cm*), Li_4OCl_2 (*I*4/*mmm*), and Li_4OBr_2 (*I*4/*mmm*). Majority of compounds that are predicted to be unstable (i.e., E_d > 0.1 eV/atom) belong to anion substitutions in the first and last half of {F, Cl, Br, I} and {O, S, Se, Te} series, respectively. Examples include *I*4/*mmm* $Li_7S_2Cl_3$ (0.147 eV/atom), *Pm*$\bar{3}$*m* Li_3TeF (0.783 eV/atom), *I*4/*mmm* $Li_7Te_2F_3$ (0.640 eV/atom), *Pmmm* $Li_8Se_2Br_3I$ (0.125 eV/atom), *P*4*mm* $Li_7SeTeFCl_2$ (0.295 eV/atom) and *Cmcm* $Li_{12}SeTe_3F_3Br$ (0.635 eV/atom).

The E_g trend is also analyzed vs. phase stability. In Fig. 3a, *ip* compounds with large E_g (> 4 eV) are noted to be highly stable as well. Three selected *in-silico* compounds are shown in Fig. 4, they contain O-Cl/I anions: n = 1 (*P*4*mm* $Li_8O_2Cl_3I$), n = 2 (*I*4*mm* $Li_7O_2Cl_2I$), and n = ∞ (*P*4/*mmm*

$Li_{12}O_4Cl_3I$). Given the large E_g values, these *ip* compounds can be categorized as good insulators, as compared relative to other known inorganic-type SEs (see Table S1). Upon inspection of the electronic band structure, the VBM is found to be dominated by O-2p states and the VBM region has highly localized peak features that corresponds well to strong ionic bonding.

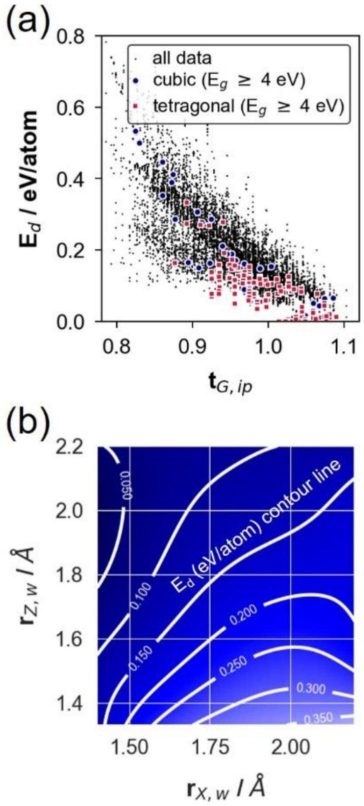

Figure 3. (a) Plot on DFT-calculated decomposition energy (E_d) vs. modified Goldschmidt tolerance factor ($t_{G,ip}$)[29] of 10,173 *in-silico* inverse perovskite (*ip*) structures in the general formulae Li_3XZ (cubic, n = ∞), Li_4XZ_2 (tetragonal, n = 1), and $Li_7X_2Z_3$ (tetragonal, n = 2). Structures with PBE electronic band gap energy (E_g) > 4 eV are highlighted in large symbols. (b) Contour map of lower-bound E_d values (per unique composition) as a function of weighted-average anion radius per formula unit ($r_{X,w}$, $r_{Z,w}$) at the X and Z site. Contour line labels indicate the E_d value.

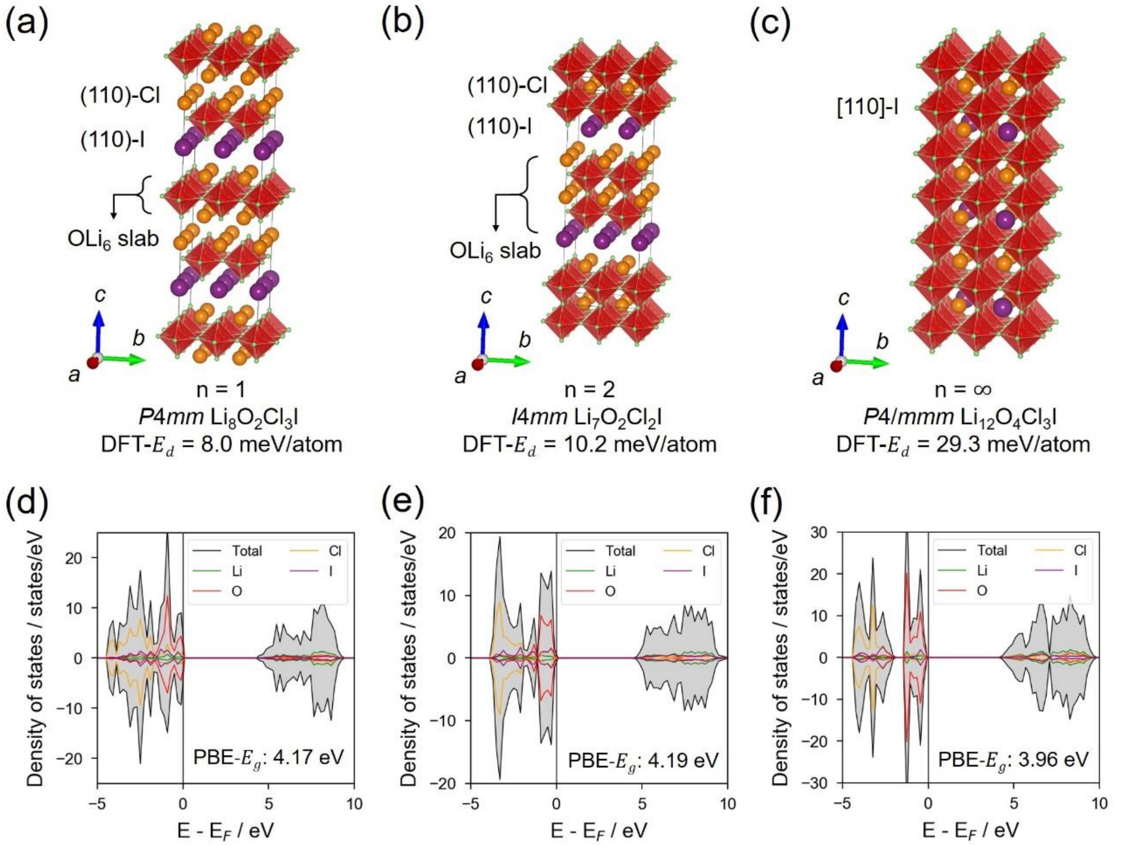

Figure 4. Representative Cl-/I-bearing *in-silico* inverse-perovskite compounds, geometry-optimized by DFT and with their (meta)stability evaluated by decomposition energy (E_d): (a) *P4mm* $Li_8O_2Cl_3I$ (n = 1 structure), (b) *I4mm* $Li_7O_2Cl_2$ (n = 2 structure), and (c) *P4/mmm* $Li_{12}O_4Cl_3I$ (n = ∞ structure). The corresponding GGA-PBE electronic density of states are shown in (d), (e), and (f), respectively.

Multiple SE-property optimization

Fig. 5a shows the MOBO-based SE screening results for *in-silico t-ip* and *c-ip* compounds, the best combination values for f_1: E_g, f_2: E_h, and f_3: Λ are plotted for each MOBO iteration step. The termination condition is achieved at the 7th step, with f_1 and f_3 determined as the fastest and slowest SE-property function, respectively. The distribution ranges are f_1 = [2.52, 4.99] eV, f_2 = [-158.27, 56.54] kJ/mol, and f_3 = [8.0 x 10^{-6}, 7.8 x 10^{-1}] S/cm. Fig. 5b depicts the Pareto-front approximation set (red-colored surface) at the 7th sampling step, containing a total of 24 optimal compounds (circle symbol) out of all the batch-sampled compounds (circle + x symbols). Table 2 summarizes Pareto-front (optimal) compounds, including their corresponding f_1, f_2, and f_3 values. The best compounds with respect to each SE-property function are *P4/nmm* $Li_8O_2Cl_3Br$ ($f_1: E_g$ = 4.99 eV), *I4/mmm* $Li_7O_2FBr_2$ ($f_2: E_h$ = 56.54 kJ/mol), and *Cmcm* $Li_{12}O_3SeClBr_3$ ($f_3: \Lambda$ = 7.8 x 10^{-1} S/cm). Oppositely, worst compounds are *Pmm*2 $Li_{12}Se_3TeBrI_3$ ($f_1: E_g$ = 2.52 eV), $Fm\overline{3}m$ Li_6O_2FCl ($f_2: E_h$ =

-158.27 kJ/mol) and *P*4*mm* $Li_8O_2ClBr_3$ (f_3: Λ = 8.0 x 10^{-6} S/cm). The small E_g of *Pmm*2 $Li_{12}Se_3TeBrI_3$ can be explained by the relatively energy-shallow anion density of states (DOS) of Se^{2-} and Te^{2-} contributions to the VB region, in converse to *P4/nmm* $Li_8O_2Cl_3Br$ (i.e., largest-E_g compound) which has O anion DOS states located in the deeper VB-region energy level. Notably, most of f_2 values are negative which indicate that H_2O reactivity in *ip* compounds is rather difficult to avoid via anion-site alloying.

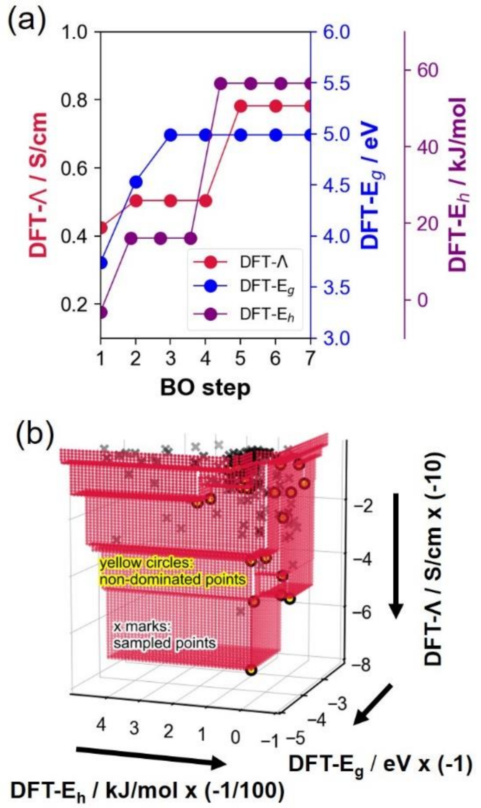

Figure 5. (a) SE-property maximization results for the *in-silico* inverse-perovskite chemical space (general formulae Li_3XZ, Li_4XZ_2, $Li_7X_2Z_3$) by multi-objective Bayesian optimization (MOBO) algorithm. SE properties include f_1: electronic band gap energy (E_g in eV), f_2: hydration energy (E_h in kJ/mol), and f_3: 400-K AIMD Li^+ ionic conductivity (Λ in S/cm). MOBO iteration is stopped when the best values of all 3 SE-property functions do not change simultaneously for 3 consecutive iterations. (b) Evolved Pareto-front approximation set (red surface) at the 7th iteration step. Arrows indicate the direction for maximization. All sampled points (compounds) are represented as x marks while non-dominated points (i.e., optimal compounds) therein are separately marked as yellow circles.

Table 2. Approximate Pareto-front (optimal) compounds derived from multiple SE-property optimization (see Figure 5). The thermodynamic (meta)stability of sampled compounds is evaluated DFT-calculated decomposition energy (E_d). Target SE properties that were simultaneously optimized are DFT-PBE electronic band gap energies (E_g), DFT reaction energy with H_2O (E_h), and AIMD bulk Li^+ ionic conductivity at 400 K (Λ).

Composition	Space group	Base structure formula	E_d / eV/atom	f_1: E_g / eV	f_2: E_h / kJ/mol	f_3: Λ / S/cm
$Li_8Te_2Br_3I$	*P*1	Li_4XZ_2 (n = 1)	0.079	3.10	+13.36	5.3 x 10^{-1}
$Li_8Se_2BrI_3$	*Cm*	Li_4XZ_2 (n = 1)	0.060	3.48	+15.45	2.2 x 10^{-1}
$Li_8O_2ClBr_3$	*P*4*mm*	Li_4XZ_2 (n = 1)	0	4.77	-21.69	8.0 x 10^{-6}
Li_8OSCl_4	*Amm*2	Li_4XZ_2 (n = 1)	0.070	4.14	-40.70	9.2 x 10^{-2}
Li_8OSCl_4	*Cmmm*	Li_4XZ_2 (n = 1)	0.077	4.12	-157.83	1.4 x 10^{-1}
$Li_8Se_2ClI_3$	*Cm*	Li_4XZ_2 (n = 1)	0.067	3.49	+15.45	4.2 x 10^{-1}
$Li_8O_2ClBr_3$	*Cm*	Li_4XZ_2 (n = 1)	0	4.53	-37.88	7.4 x 10^{-2}
$Li_8O_2Cl_3Br$	*Cm*	Li_4XZ_2 (n = 1)	0	4.74	-33.22	9.0 x 10^{-4}
$Li_8O_2Cl_3Br$	*P*4/*nmm*	Li_4XZ_2 (n = 1)	0	4.99	-39.39	1.0 x 10^{-5}
$Li_8S_2Cl_3I$	*Cm*	Li_4XZ_2 (n = 1)	0.059	4.11	+7.06	3.3 x 10^{-1}
$Li_7O_2FBr_2$	*I*4/*mmm*	$Li_7X_2Z_3$ (n = 2)	0.074	4.24	+56.54	5.0 x 10^{-5}
$Li_7O_2Cl_2Br$	*P*4/*nmm*	$Li_7X_2Z_3$ (n = 2)	0	4.62	-22.49	3.0 x 10^{-3}
Li_3OCl	$Pm\bar{3}m$	Li_3XZ (n = ∞)	0	4.56	-22.43	4.8 x 10^{-2}
Li_6O_2FCl	$Fm\bar{3}m$	Li_3XZ (n = ∞)	0.091	4.65	-158.27	1.3 x 10^{-1}
Li_6O_2ClBr	$Fm\bar{3}m$	Li_3XZ (n = ∞)	0.009	4.36	-31.99	8.2 x 10^{-2}
$Li_6SSeClI$	*Pmm*2	Li_3XZ (n = ∞)	0.076	3.12	+16.12	1.4 x 10^{-1}
$Li_9O_3ClBr_2$	*P*4/*mmm*	Li_3XZ (n = ∞)	0.011	4.96	-34.66	9.0 x 10^{-3}
$Li_9O_2SBr_2I$	*P*4*mm*	Li_3XZ (n = ∞)	0.086	3.90	-51.46	3.6 x 10^{-1}
$Li_{12}OS_3Cl_2Br_2$	*Amm*2	Li_3XZ (n = ∞)	0.077	3.74	+8.35	1.2 x 10^{-1}
$Li_{12}OS_3Cl_2Br_2$	*Pm*	Li_3XZ (n = ∞)	0.072	3.54	-66.74	5.2 x 10^{-1}
$Li_{12}SSe_3ClI_3$	*Cmmm*	Li_3XZ (n = ∞)	0.096	3.28	-1.73	5.0 x 10^{-1}
$Li_{12}Se_3TeBrI_3$	*Pmm*2	Li_3XZ (n = ∞)	0.094	2.52	+18.99	1.3 x 10^{-1}
$Li_{12}O_3SeClBr_3$	*Cmcm*	Li_3XZ (n = ∞)	0.097	3.36	-86.88	7.8 x 10^{-1}
Li_6OSeI_2	$Fm\bar{3}m$	Li_3XZ (n = ∞)	0.059	3.10	+38.42	3.8 x 10^{-2}

Electrochemical window analysis

Fig. 6 shows the DFT-calculated Li grand potential phase stability plots for various Li-rich inverse-perovskite (*ip*) solid electrolyte (SE) candidates with various anion-site substitutions as shown below; decomposition product phases in different voltage ranges are indicated.[68] It is noted that the most of the SE candidates are predicted to be metastable (i.e., E_d < 0.1 eV/atom). Given this, when in contact with the Li metal anode, the thermodynamic decomposition phases are expected to be the relevant phases to constitute the interphase region between the anode and the SE component. Consequently, the electrochemical window of the SE candidates may be considered as interphase-controlled. Meanwhile, a crucial consideration of the interphase region is that it should be Li-ion conducting but electronically insulating at the same time, so that further decomposition of the (kinetically stabilized) main-bulk SE component, as well as Li dendrite growth during the Li plating process (i.e., during battery charging), can be prevented.

For example, the relevant decomposition phases for *P*1 $Li_8Te_2Br_3I$ SE are LiI, LiBr, and Li_2Te (see Figure (a)) in the electrochemical window of [0 V, 1.56 V]. Experimentally, LiI has been reported as a good Li ion conductor, while LiBr was shown to have a beneficial Li dendrite suppression effect.[69,70] On the other hand, Li_2Te has been predicted by DFT to have a low bulk Li ion activation energy.[71] Overall, the interphase region formed by the 3 phases is predicted to provide a favorable Li ion transport between Li metal anode and $Li_8Te_2Br_3I$ SE. A similar analysis can be performed as well for the other SE compounds, such as *Cm* $Li_8S_2Cl_3I$ (LiI, LiCl, and Li_2S in the range of [0 V, 2.34 V]), $Fm\bar{3}m$ Li_6O_2ClBr (Li_2O, LiBr, and LiCl in the range of [0 V, 2.79 V]), *Pmm*2 $Li_6SSeClI$ (LiI, Li_2Se, Li_2S, and LiCl in the range of [0 V, 1.89 V]), *Pmm*2 $Li_{12}Se_3TeBrI_3$ (Li_2Te, LiI, LiBr, and Li_2Se in the range of [0 V, 1.56 V]), and $Fm\bar{3}m$ Li_6OSeI_2 (Li_2O, Li_2Se, and LiI in the range of [0 V, 1.89 V]). Among the decomposition phases of these *ip* SEs, Li_2S poses a detrimental effect for the interphase region because of its poor Li ionic conductivity of ~10^{-13} S/cm at room temperature.[72] As a consequence, S-bearing *ip* compositions such as *Cm* $Li_8S_2Cl_3I$ and *Pmm*2 $Li_6SSeClI$ may not form an interphase region with high Li ion diffusivity across the anode - SE interface.

A notable observation for the oxidative stability (i.e., at low Li chemical potential condition) of *ip* SE compounds is that the interphase-controlled voltage window for O-bearing compositions are generally larger than for non-O-bearing ones, such as in the case of $Fm\bar{3}m$ Li_6O_2ClBr ([0 V, 2.79 V]) vs. $Li_{12}Se_3TeBrI_3$ ([0 V, 1.56 V]). Collectively, an oxidative stability trend down the periodic table of elements can be deduced: $O^{2-} > S^{2-} > Se^{2-} > Te^{2-}$. We emphasize that this trend is also consistent with the observed trend for the DFT electronic band gap energy (E_g) which was used as an electrochemical window upper bound for *ip* SEs (see Figure 3a).

Based on above thermodynamic analysis, *ip* SEs generally exhibit narrow electrochemical stability windows. However, they can be effectively extended by the decomposition phases that form the interphase.[73] Thus, the wide electrochemical window that was demonstrated experimentally in a prior work using an *ip* SE may have stemmed from the interphase compounds at the SE-electrode interface.[23]

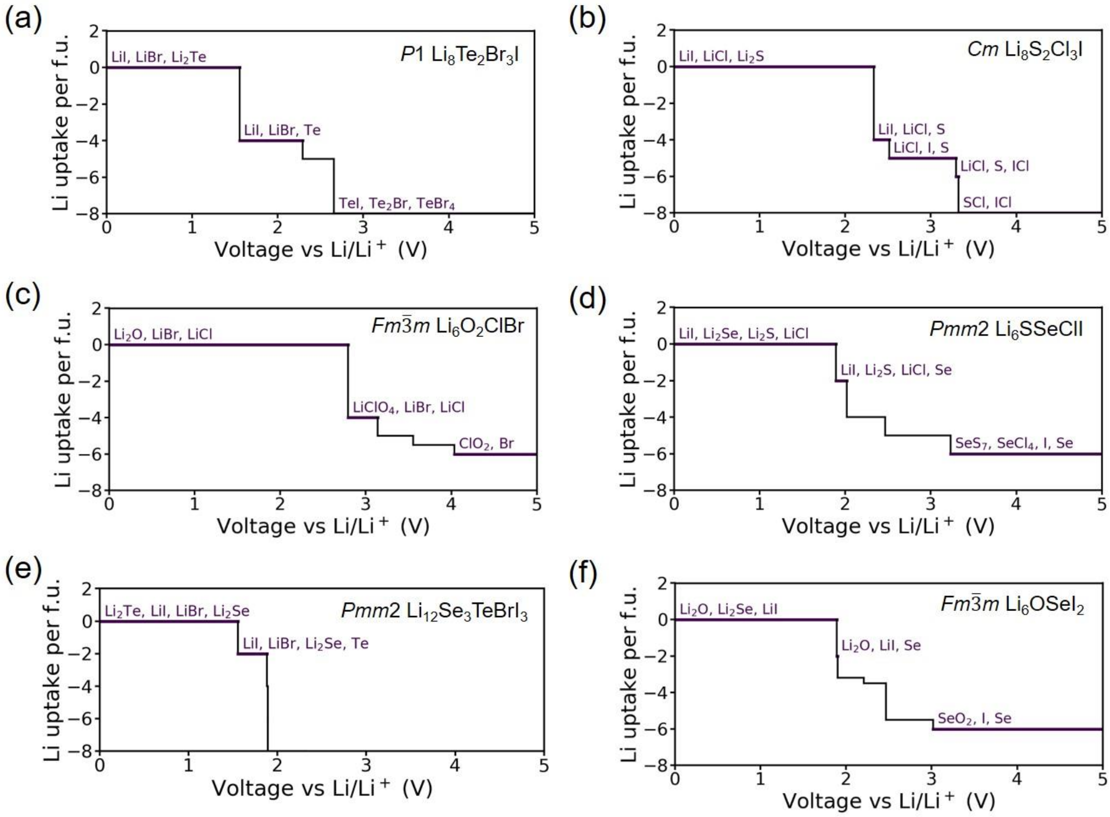

Figure 6. Li grand potential phase stability plots for selected Li-rich inverse-perovskite (*ip*) solid electrolyte (SE) candidates from Table 2: (a) $P1$ $Li_8Te_2Br_3I$, (b) Cm $Li_8S_2Cl_3I$, (c) $Fm\bar{3}m$ Li_6O_2ClBr, (d) $Pmm2$ $Li_6SSeClI$, (e) $Pmm2$ $Li_{12}Se_3TeBrI_3$, and (f) $Fm\bar{3}m$ Li_6OSeI_2. In the anodic or low voltage region, the decomposition binary phases determine the reductive stability, whereas in the cathodic or high voltage region (i.e., after the first step in the Li uptake axis), they are predicted to undergo oxidation and loses Li. Compounds listed in the plots are DFT-predicted phase equilibria (decomposition phases) at corresponding voltage regions (V vs Li/Li$^+$).

The stability of *ip* SEs when in contact with known cathode materials were evaluated by calculating the interfacial mutual reaction energy. Specifically, the reaction energy minimum ($\Delta E_{mutual,min}$) with respect to varying reaction ratio of the cathode and the SE was calculated using an approach employed in a previous work:[68]

$$\Delta E_{mutual,min} = \min_{x\in[0,1]} \left\{ \frac{1}{N} \left[E_{eq}(xc_A + (1-x)c_{SE}) - xE(c_A) - (1-x)E(c_{SE}) \right] \right\}, \qquad (25)$$

where x is the ratio of cathode A, $E(c_A)$ and $E(c_{SE})$ are the DFT-calculated total energies at the convex hull at the composition of cathode A and SE, respectively, N is the total number of atoms involved in the reaction, and $E_{eq}(xc_A + (1-x)c_{SE})$ is the phase equilibria energy at composition $xc_A + (1-x)c_{SE}$. Fig. 7a shows the pseudobinary phase diagram on $\Delta E_{mutual,min}$ of several *ip* SE candidates when in contact with the NMC811 cathode ($LiNi_{10/12}Mn_{1/12}Co_{1/12}O_2$). Among the *ip* SEs, S-, Se- and Te-bearing compositions are predicted to have the highest reactivity. For instance, the reaction energy between *Pm* $Li_{12}OS_3Cl_2Br_2$ SE and NMC811 is -270 meV/atom. This result is in good agreement with our previous DFT-based study on the possible reactions and structures at the solid hetero-interface formed between an oxide-type cathode ($LiCoO_2$) and a sulfide-type SE (β-Li_3PS_4), in which the O-S exchange reaction across the interface was predicted to be thermodynamically favorable.[72] On the other hand, O-bearing compositions show the lowest reactivity, such as in the case of *P*4*mm* $Li_9O_3ClBr_2$ which is only -7 meV/atom. Extending to other Ni-Mn-Co compositions (see Fig. 7b), it is evident that the interfacial reactivity of *ip* SEs are positively correlated with Ni content, with $LiNiO_2$ (i.e., 100% Ni at the transition metal site of the layered structure) showing the most exothermic reactions (i.e., darkest-colored heatmap cells). The $LiFePO_4$ cathode generally shows a relatively moderate reactivity vs. *ip* SEs, the reaction energy range is between -120 and -70 meV/atom. For the $LiCoO_2$ cathode, O-bearing *ip* SEs show low reactivity (above -10 meV/atom), while the rest have moderate reactivity (-90 to -10 meV/atom). The least reactive cathode (i.e., with the lightest-colored heatmap cells) vs. *ip* SEs is $LiMnO_2$, with reaction energies that are very close to 0. This predicted interfacial stability is consistent with the findings of a previous DFT work,[75] it was suggested to have stemmed from the relative stability of the oxidation state of Mn as compared to Ni and Co.

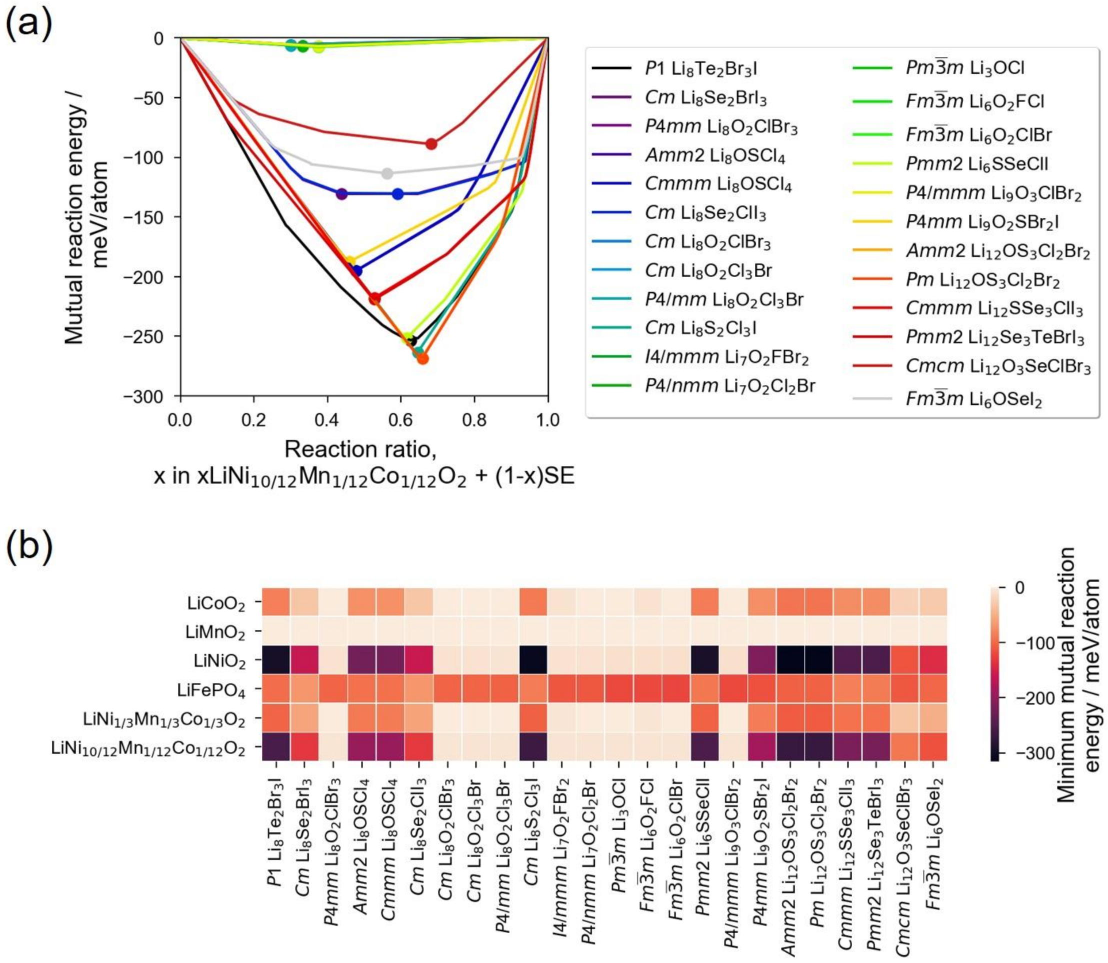

Figure 7. (a) DFT-calculated pseudobinary phase diagram of NCM811 cathode ($LiNi_{10/12}Mn_{1/12}Co_{1/12}O_2$) that is in contact with Li-rich inverse-perovskite (*ip*) solid electrolyte (SE) candidates that are listed in Table 2 (the same compound ordering). The circle markers indicate the most exothermic reactions (i.e., most negative reaction energy) at a given cathode-SE reaction ratio. (b) Mutual reaction energy heatmap between known cathode materials and *ip* SEs that are listed in Table 2 (again, the same compound ordering).

Li^+ *ion transport analysis*

Bulk Li^+ ionic conductivity (σ_{bulk}) can be largely affected by defects in the as-prepared SE material. Here, we investigate the σ_{bulk} of *t-ip* and *c-ip* compounds by deriving the Arrhenius plot from multiple AIMD temperatures. Two defect-driven Li^+ ion transport processes are separately investigated: Li-interstitial and Li-vacancy mechanism. Fig. 8a shows the σ_{bulk} plot for selected compounds from Table 1: *Cm* $Li_8S_2Cl_3I$ (n = 1 structure), *Cmcm* $Li_{12}O_3SeClBr_3$ (n = ∞ structure), and *P*4/*nmm* $Li_7O_2Cl_2Br$ (n = 2 structure). Moreover, the nature of the diffusion channels is displayed in Fig. 8b and 8d for the tetragonal symmetry (*Cm* $Li_8S_2Cl_3I$ and *P*4/*nmm* $Li_7O_2Cl_2Br$) and in Fig. 8c for the cubic symmetry (*Cmcm* $Li_{12}O_3SeClBr_3$). It is noted that the Li ion diffusion of *ip* compounds with the tetragonal structure has a low Li ion migration barrier within the intra-slab-layer, while the inter-slab-layer migration has a large energy barrier, as demonstrated in our previous work by DFT climbing-image nudged elastic band method.[29] The large energy barrier for the inter-slab Li ion migration is characterized by a transition state in which Li ions need to pass between two halide anions. On the other hand, the energetically favorable intra-slab layer migration has a transition state which can be described by a triangular plane with vertices formed by one O^{2-}/S^{2-} anion and two halide anions. In the case of cubic *Cmcm* $Li_{12}O_3SeClBr_3$ (Figure 8c), the slab layer size in the vertical direction is effectively infinite ($n = \infty$) and all the local transition states are similar (i.e., a triangular plane with vertices formed by one O^{2-}/Se^{2-} anion and two halide anions). Thus, the Li ion diffusion is relatively more percolated in 3D in the cubic structure than in the tetragonal structure.

Based on the σ_{bulk}T vs. 1000/T slope, it is evident that the Li-interstitial mechanism generally results in a relatively higher conductivity than the Li-vacancy case. This can be explained by the increased Li-Li repulsion effect due to shorter effective Li-Li interatomic distance (Fig. S2) that leads to Li site-potential shallowing, such as in the case of garnet-type $Li_7La_3Zr_2O_{12}$ SE.[76,77] Therefore, it would be beneficial to stabilize this defect type, such as through stoichiometry control during synthesis (e.g., by excess X^{2-} anion into the halide Z^- anion site). Some optimization efforts have been made in related compositions, but they were focused on introducing Li vacancies, such as in Ba-doped Li_3OCl and Li-Cl Frenkel defects in Li_3OCl.[23,78] Estimates on E_a in Fig. 6a with Li-interstitial (Li-vacancy) mechanism are 0.15 (0.27), 0.37 (0.42) and 0.33 (0.50) eV, respectively. The lowest E_a of the three compounds, which is for *Cm* $Li_8S_2Cl_3I$, can be traced to the highly polarizable S^{2-} anions which promote noticeable tilting of the linked anion-center SLi_6 octahedral units in the geometry-optimized structure (see Fig. 8b). This degree of tilting correlates with the extent of the displacement amplitude of Li^+ ions within their site cages and around the S^{2-} anion, as qualitatively exhibited by the locally wider Li trajectory densities, as compared to the other selected compounds which have the less-polarizable O^{2-} anions (Fig. 8c, 8d).

While the local Li pathway characteristics are shown to depend on anion chemistry, the structure type determines the diffusion dimensionality in *ip* structures. Specifically, Li^+ ion diffusion in the *t-ip* structure (n = 1, 2) proceeds in a 2D manner, confined within each *ip* slab layer units. Although interstitial sites exist in the interslab region, these sites are apparently inaccessible for a migrating Li^+ ion because of a large energy barrier.[29] On the other hand, *c-ip* compounds generally have 3D diffusion, with contiguous Li site connectivity via corner-linking of anion-center XLi_6 octahedral units.

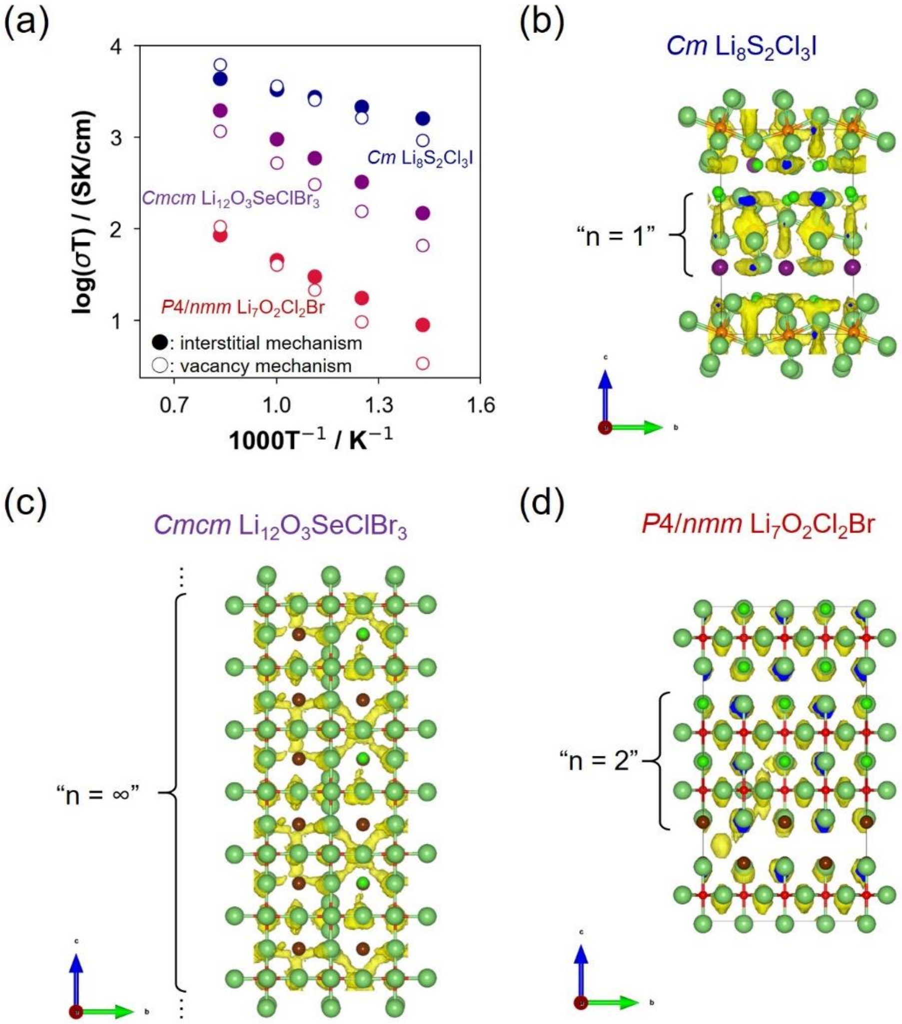

Figure 8. (a) Conductivity plot of 3 novel inverse-perovkite (*ip*) compounds (*Cm* $Li_8S_2Cl_3I$, *Cmcm* $Li_{12}O_3SeClBr_3$, *P*4/*nmm* $Li_7O_2Cl_2Br$) based on Li-interstitial and Li-vacancy mechanism. The corresponding Li^+ ion trajectory densities (in yellow, with cross-section in blue) as derived by 400-K NVT-AIMD runs are shown in (b)-(d), respectively; bondings within the *ip* structures are displayed in anion-center view. The *ip* slab size are indicated by parameter n which is 1, 2, ∞ for the Li_4XZ_2, $Li_7X_2Z_3$ and Li_3XZ parent structure, respectively.

Evaluation of synthesis likelihood

Although E_d has been shown in the past to be valid when predicting the phase stability of experimentally confirmed compounds, it cannot fully ascertain beforehand whether theoretically designed compounds are really synthesizable or not. This is expected, given the complexity and variability involved when actually synthesizing compounds in the lab. To supplement E_d in evaluating the synthesis likelihood of *in-silico ip* compounds in this work, an additional stability parameter is considered. This parameter is determined from a deep-learning (DL) model that is trained on a structure dataset that is composed of positive (synthesizable) and negative (virtual or unsynthesized) compound entries from the Materials Project (MP) database; there are 46,781 entries that are originally from the ICSD database and 77,734 entries that are virtually generated ones.[79] Essentially, the DL model performs a positive-unlabeled (semi-supervised) classification task, using descriptors that are derived from crystal graph network representation. The stability parameter is then expressed as a probability "crystal-likeness" score (L_s). If $L_s > 0.50$, a given compound is considered as sufficiently alike in terms of crystal structure as with known experimental compounds, otherwise L_s is too low and the compound tag is set to 'unlabeled' (i.e., ambiguous).

Fig. 9a displays the L_s vs. E_d plot for 10,173 *in-silico t-ip* and *c-ip* compounds. Four regions of interest are shown based on the (dis)agreement between the two parameters: (1) $L_s > 0.5$ and $E_d <$ 0.1 eV/atom, (2) $L_s > 0.5$ and $E_d >$ 0.1 eV/atom, (3) $L_s < 0.5$ and $E_d <$ 0.1 eV/atom, and (4) $L_s < 0.5$ and $E_d >$ 0.1 eV/atom. A continuous L_s distribution is also found, described with statistical range, mean, and skewness of [0.025, 0.909], 0.542 and -0.395, respectively; the negative skew implies that the median L_s is larger than the mean L_s which, is in turn, lies in the 'synthesizable' regime. About 61.25% (i.e., 6,231/10,173) are labeled as 'synthesizable' (regions 1 and 2), with 13.89% (1,413/10,173) labeled as both 'synthesizable' and thermodynamically (meta)stable (region 1). Meanwhile, 47.43% (4,825/10,173) are labeled as 'synthesizable' but are predicted to be thermodynamically unstable E_d criterion (region 2). In contrast, only 0.86% (88/10,173) are labeled as 'ambiguous' compounds, even though they are DFT-predicted to be (meta)stable (region 3). Lastly, 37.70% (3,835/10,173) are predicted as 'ambiguous' and unstable (region 4). Out of the four regions, region 1 (i.e., $L_s > 0.5$ and $E_d <$ 0.1 eV/atom) is of particular interest, it further excludes 1,501 (by E_d) – 1,413 (by L_s) = 88 compounds in terms of priority towards actual synthesis. In Fig. 9b, the breakdown of counted compounds and composition-stability relationship for region 1 is shown. The stability trend is found to be consistent with trends based on E_d and $t_{G,ip}$. Specifically, the order of decreasing stability is reflected by the compound counts: O^{2-} → S^{2-} → Se^{2-} → Te^{2-} and I^- → Br^- → Cl^- → F^-. Interestingly, L_s is shown to have a moderately negative correlation vs. E_d, indicating that it partly captured the information on thermodynamic stability despite the DL model not being explicitly trained on the E_d dataset. The list of region-1 compounds is provided in the Supporting information (Table S2), including their L_s and E_d values. Overall, the combined synthesizability parameters L_s and E_d should provide experimentalists with a well-informed list of compounds for actual synthesis.

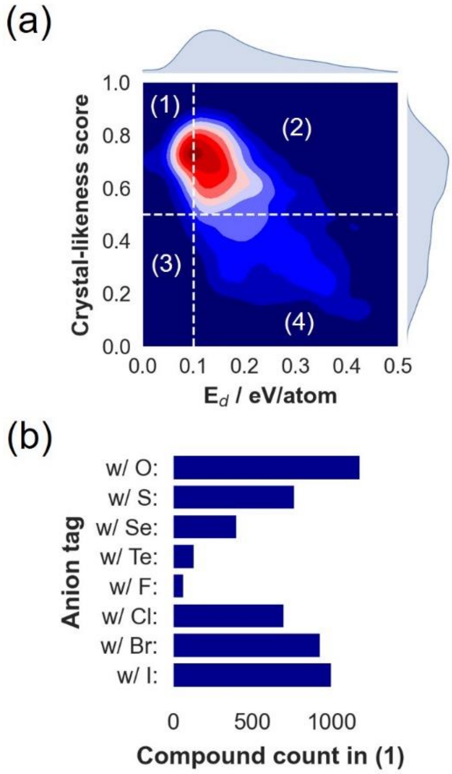

Figure 9. (a) Synthesis likelihood (L_s) map by crystal-likeness (CL) score and thermodynamic decomposition energy (E_d) plot for 10,173 *in-silico* inverse-perovskite (*ip*) compounds. The CL score was determined by a trained deep learning model on experimental and virtual compounds from Materials Project.[79] The CL score indicates the label probability of a compound as either 'synthesizable' or 'ambiguous' (i.e., either synthesizable or not). The criterion for synthesis likelihood and thermodynamic stability were set to $L_s > 0.50$ (horizontal line) and $E_d < 0.1$ eV/atom (vertical line), respectively. Four regions of interest are shown, grouping compounds with: (1) $L_s > 0.5$ and $E_d < 0.1$ eV/atom, (2) $L_s > 0.5$ and $E_d > 0.1$ eV/atom, (3) $L_s < 0.5$ and $E_d < 0.1$ eV/atom, and (4) $L_s < 0.5$ and $E_d > 0.1$ eV/atom. (b) Anion-specific composition counts for region (1) in (a).

Analysis on solid-state synthesis pathways

Synthesis reaction pathways can vary largely depending on experimental conditions (e.g., reaction energies, competing phases, nucleation barriers, reactant mixing homogeneity, heating protocol, and choice of starting reactants/precursors). To this end, the solid-state synthesis routes of *in-silico t-ip* and *c-ip* compounds are studied using a data-driven approach that is based on classical nucleation theory (CNT).[80] The method starts with the description of steady-state CNT for a given reaction with solid reactants α_i (where $i = 1, 2, 3, \ldots$). The heterogeneous nucleation rate (J) of a target phase β (i.e., the *in-silico ip* compound in this work) on the surface of a reactant α_i at temperature T is given by:

$$J_{\alpha_i \rightarrow \beta} = J_0 e^{\left[-\Delta G^*_{\alpha_i \rightarrow \beta}/k_B T\right]}, \tag{26}$$

where J_0 is the pre-exponential factor and $\Delta G^*_{\alpha_i \rightarrow \beta}$ is the critical thermodynamic nucleation barrier. For a spherical nucleus, the latter can be expressed as follows:

$$\Delta G^*_{\alpha_i \rightarrow \beta} = \frac{16\pi\gamma_\beta^3 f\left(S_{\alpha_i \rightarrow \beta}\right)}{3(\Delta G)^2}, \tag{27}$$

where γ_β is the surface energy of phase β, ΔG is the reaction free energy per volume of the formed cluster phase β, and $f\left(S_{\alpha_i \rightarrow \beta}\right)$ is the factor for barrier reduction (in the range of [0, 1]) from the homogeneous or uncatalyzed limit on the surface of reactant α_i as a function of $S_{\alpha_i \rightarrow \beta}$ which is the cosine of the contact angle (θ) between reactant substrate α_i and target phase β:

$$S_{\alpha_i \rightarrow \beta} = \cos\theta_{\beta\alpha_i} = \frac{\gamma_{\alpha_i} - \gamma_{\beta\alpha_i}}{\gamma_\beta}, \tag{28}$$

where γ_{α_i} and $\gamma_{\beta\alpha_i}$ are the surface energy of substrate α_i and the interface energy between the substrate α_i and nucleus β. The expression for $f\left(S_{\alpha_i \rightarrow \beta}\right)$ is formulated as a monotonic function:

$$f\left(S_{\alpha_i \rightarrow \beta}\right) = \frac{2 - 3S_{\alpha_i \rightarrow \beta} + S^3_{\alpha_i \rightarrow \beta}}{4}. \tag{29}$$

For the purpose of simply distinguishing the favorable reactions from non-favorable ones, $S_{\alpha_1 \rightarrow \beta}$ is approximated based on crystal structure similarity and epitaxial matching arguments follows:

$$S_{\alpha_1 \rightarrow \beta} = 1 - q^{sim}_{\alpha_i,\beta} - q^{epi}_{\alpha_i,\beta}, \tag{30}$$

where $q^{sim}_{\alpha_i,\beta}$ and $q^{epi}_{\alpha_i,\beta}$ are normalized distance metrics (scaled to [0, 1]). Meanwhile, the overall reaction barrier ($\Delta G^{**}_{\alpha_i \rightarrow \beta}$) was formulated with the inclusion of the reaction activation barrier ($\Delta E_{\alpha_i \rightarrow \beta}$, which is contained in J_0):

$$\Delta G^{**}_{\alpha_i \rightarrow \beta} = \Delta G^*_{\alpha_i \rightarrow \beta} + \Delta E_{\alpha_i \rightarrow \beta}. \tag{31}$$

Here, the structure similarity parameter $q^{sim}_{\alpha_i,\beta}$ was used to approximate $\Delta E_{\alpha_i \rightarrow \beta}$ (i.e., $\Delta E_{\alpha_i \rightarrow \beta} \propto q^{sim}_{\alpha_i,\beta}$). Finally, the minimum heterogeneous nucleation barrier (ΔG^{**}) for a given candidate reaction to form β was determined among m reactants:

$$\Delta G^{**} = \min\left\{\Delta G^{**}_{\alpha_1 \rightarrow \beta}, \Delta G^{**}_{\alpha_2 \rightarrow \beta}, \ldots, \Delta G^{**}_{\alpha_m \rightarrow \beta}\right\}. \tag{32}$$

From above formulations, candidate solid-state reactions for the *in-silico ip* compounds can be searched based on: i) heterogeneous nucleation barriers (that can be estimated using high-throughput thermochemical data) and ii) the number of competing phases aside from the target compound to be synthesized. Using these two parameters, optimal reaction pathways can be identified by Pareto analysis, with the goal of finding reactions that both have the lowest barrier and the fewest number of competing phases. For this analysis, the reaction temperature and pressure are set to 1000 K and 1 atm, respectively. Included in the reactant list are binary powders (e.g., Li_2O, LiCl, LiBr, Li_2O_2), carbon-containing precursors (e.g., Li_2CO_3, C), elemental solids (e.g., Li, I), and O_2 gas. Reactants with known extreme toxicity (e.g., SeO_2, CCl_4, $SeBr_4$) are excluded.

Fig. 10 displays the 2D Pareto plots of possible synthesis pathways of representative *t-ip* and *c-ip* compounds. It includes 2 experimentally confirmed compounds ($Pm\bar{3}m$ Li_3OCl and $I4/mmm$ Li_4OBr_2) and yet-to-be synthesized metastable candidates ($P4/nmm$ $Li_8O_2Cl_3Br$, $I4/mmm$ $Li_7O_2FBr_2$, $Fm\bar{3}m$ Li_6OSeI_2, and $Cmcm$ $Li_{12}O_3SeClBr_3$). Each data point in the subplots represents a possible reaction route (Table S3-S8). The dashed lines (in red) show the Pareto-frontier of non-dominated data points (i.e., optimal reaction routes for a given target compound). Table 3 shows the detailed reactions for the compounds shown in Fig. 10.

For $Pm\bar{3}m$ Li_3OCl, the route with the fewest number of competing phases is the reaction using Li_2O_2 and LiCl (i.e., Δ_1 with 2 competing phases). Meanwhile, for a combustion-type reaction (i.e., with a C source), the nucleation barrier is predicted to decrease down to a quarter (i.e., 3.72 → 0.78 a.u.), but this route can increase the number of competing phases (e.g., Δ_2 with 3 competing phases). Replacing LiCl with ClO_x precursors can also further reduce the nucleation barrier, but also at the expense of further increased number of competing phases.

For $I4/mmm$ Li_4OBr_2, one reaction route (Δ_3) can completely avoid the formation of competing phases, but it has a very large nucleation barrier (44.2×10^3 a.u.). Using a catalytic-type reaction (e.g., using C, Li_2O_2, and LiBr as reactants), the barrier is largely reduced by 4 orders of magnitude (Δ_4, $44.2 \times 10^3 \rightarrow 1.22$ a.u.) but it can facilitate the formation of 2 competing phases. Replacing the Br source from LiBr to Br_2O_3, the barrier further reduces by another factor but the formation of more competing phases is predicted.

For $P4/nmm$ $Li_8O_2Cl_3Br$, Pareto-front reactions all involve a C source and CO_2 release. A relatively moderate kinetic barrier magnitude is predicted (12.06 a.u.) for a reaction involving Li_2CO_3, LiBr, and LiCl; this reaction results to 2 competing phases (Δ_5). A reduction of the barrier by 2 orders of magnitude is predicted (12.06 → 0.30 a.u.) with using 4 reactants (Li_2O, LiBr, LiC_{12}, and $LiClO_4$), though the number of competing phases is increased to 3 (Δ_6).

For $I4/mmm$ $Li_7O_2FBr_2$, the reaction route which assisted by Li_2CO_3 (with LiBr and LiF) only leads to 1 competing phase (Δ_7) and the nucleation barrier is relatively moderate (16.31 a.u.). If Li_2CO_3 is replaced with C and Li_2O_2, the barrier is reduced by 2 orders of magnitude (16.31 → 0.84 a.u.), but the number of competing phases increases to 2 (Δ_8). Other reaction routes, such as those involving with reactants Li_2O and Br_2O_3, slightly reduce the kinetic barrier but they are accompanied with the further increase in the number of competing phases.

For $Fm\bar{3}m$ Li_6OSeI_2, one route does not result to the appearance of competing phases (Δ_8) and with a relatively low nucleation barrier (0.11 a.u.). This reaction is involved with 4 reactants such as Li_2CO_3, Li_2Se, LiC_{12} and $LiIO_3$. Changing the reactant types and their combination only increases the number of competing phases.

For $Cmcm$ $Li_{12}O_3SeClBr_3$, all Pareto-based reactions (e.g., Δ_{10} and Δ_{11}) are involved with 5 reactants and with relatively low nucleation barrier (0.10 a.u.), though the number of competing phases is at least 3. These reaction outcomes are rather intuitive, given the complex composition of the target phase (i.e., 5-element system).

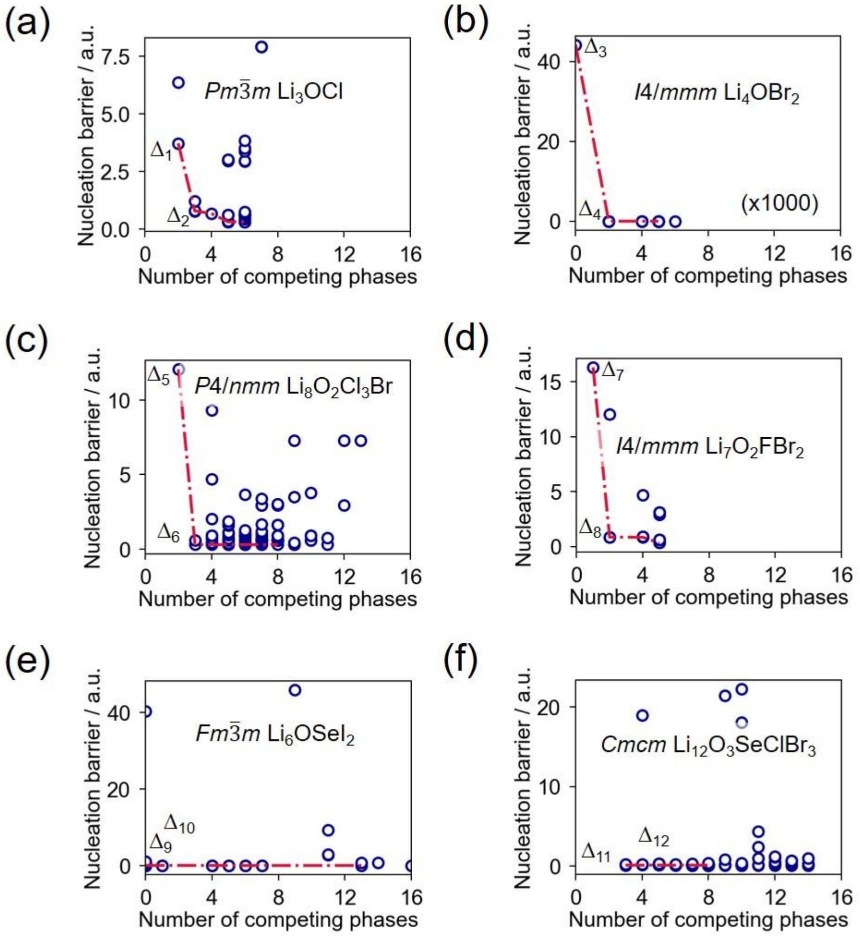

Figure 10. Analysis on solid-state synthesis reaction pathways (at 1000 K, 1 atm) of screened inverse-perovskite (*ip*) compounds (see Table 2): (a) $Pm\overline{3}m$ Li_3OCl, (b) $I4/mmm$ Li_4OBr_2, (c) $P4/nmm$ $Li_8O_2Cl_3Br$, (d) $I4/mmm$ $Li_7O_2FBr_2$, (e) $Fm\overline{3}m$ Li_6OSeI_2, and (f) $Cmcm$ $Li_{12}O_3SeClBr_3$. The analysis was performed using a heuristic approach based on classical nucleation theory and temperature-dependent Gibbs reaction energy (as described in ref. 80). Red dashed lines indicate Pareto frontiers for the 2 objective functions: nucleation barrier and number of competing phases. Competing phases are compounds which form using the same precursor sets as the target *ip* compound. Competing phases determined from Gibbs free energy calculations for ternary, quaternary, and quinary *ip* compounds were searched to include {binary}, {binary, ternary}, and {binary, ternary, quaternary} phases, respectively. Selected (Pareto-frontier) reaction routes are labeled (Δ_1, Δ_2, etc.). Nucleation barrier in (b) is normalized by a factor of 1000 for visual clarity.

Table 3. Summary of possible synthesis reaction pathways for selected inverse perovskite (*ip*) compounds based on Pareto analysis with 2 objective functions: number (#) of competing phases and

approximated nucleation barrier (method according to ref. 80). The list includes 2 experimentally confirmed compounds ($Pm\bar{3}m$ Li_3OCl, $I4/mmm$ Li_4OBr_2) and 4 yet-to-be synthesized ones ($P4/nmm$ $Li_8O_2Cl_3Br$, Cm $Li_8S_2Cl_3I$, $Fm\bar{3}m$ Li_6OSeI_2, $Cmcm$ $Li_{12}O_3SeClBr_3$). Reaction routes (labeled as Δ_i) correspond to the same labels in Fig. 8 insets.

Target compound	#competing phases	Nucleation barrier / a.u.	Pareto-front reaction routes
$Pm\bar{3}m$ Li_3OCl	2	3.72	$Li_2O_2 + LiCl \rightarrow Li_3OCl + 0.5\ O_2$ (Δ_1)
	3	0.78	$0.5\ C + Li_2O_2 + LiCl \rightarrow Li_3OCl + 0.5\ CO_2$ (Δ_2)
	4	0.68	$ClO_2 + 1.5\ Li_2O \rightarrow Li_3OCl + 1.25\ O_2$
	5	0.32	$1.0\ ClO_3 + 1.4286\ Li_2O + 0.1429\ LiC_{12} \rightarrow Li_3OCl + 1.7143\ CO_2$
	6	0.31	$0.5\ Cl_2O_7 + 1.4184\ Li_2O + 0.1633\ LiC_{12} \rightarrow Li_3OCl + 1.9592\ CO_2$
$I4/mmm$ Li_4OBr_2	0	44.2 x 10^3	$Li_2O + 2.0\ LiBr \rightarrow Li_4OBr_2$ (Δ_3)
	2	1.22	$0.5\ C + Li_2O_2 + 2.0\ LiBr \rightarrow Li_4OBr_2 + 0.5\ CO_2$ (Δ_4)
	4	0.81	$Br_2O_3 + 2.0\ Li_2O \rightarrow Li_4OBr_2 + 2.0\ O_2$
	5	0.34	$Br_2O_3 + 1.9184\ Li_2O + 0.1633\ LiC_{12} \rightarrow Li_4OBr_2 + 1.9592\ CO_2$
$P4/nmm$ $Li_8O_2Cl_3Br$	2	12.06	$2.0\ Li_2CO_3 + LiBr + 3.0\ LiCl \rightarrow Li_8O_2Cl_3Br + 2.0\ CO_2$ (Δ_5)
	3	0.30	$1.7551\ Li_2O + LiBr + 0.4898\ LiC_{12} + 3.0\ LiClO_4 \rightarrow Li_8O_2Cl_3Br + 5.8776\ CO_2$ (Δ_6)
	8	0.30	$0.5\ Br_2O_3 + 2.2143\ Li_2O + 0.5714\ LiC_{12} + 3.0\ LiClO_4 \rightarrow Li_8O_2Cl_3Br + 6.8571\ CO_2$
$I4/mmm$ $Li_7O_2FBr_2$	1	16.31	$2.0\ Li_2CO_3 + 2.0\ LiBr + LiF \rightarrow Li_7O_2FBr_2 + 2.0\ CO_2$ (Δ_7)
	2	0.84	$C + 2.0\ Li_2O_2 + 2.0\ LiBr + LiF \rightarrow Li_7O_2FBr_2 + CO_2$ (Δ_8)
	4	0.84	$Br_2O_3 + 3.0\ Li_2O + LiF \rightarrow Li_7O_2FBr_2 + 2.0\ O_2$
	5	0.33	$Br_2O_3 + 2.9184\ Li_2O + 0.1633\ LiC_{12} + LiF \rightarrow Li_7O_2FBr_2 + 1.9592\ CO_2$
$Fm\bar{3}m$ Li_6OSeI_2	0	0.12	$0.8776\ Li_2CO_3 + Li_2Se + 0.2449\ LiC_{12} +$

			$2.0\ LiIO_3 \rightarrow Li_6OSeI_2 + 3.8163\ CO_2$ (Δ_8)
	1	0.11	$3.5\ C + Li_2O_2 + Li_2Se + 2.0\ LiIO_3 \rightarrow Li_6OSeI_2 + 3.5\ CO_2$ (Δ_9)
	5	0.11	$I_2O_5 + 1.8776\ Li_2CO_3 + Li_2Se + 0.2449\ LiC_{12} \rightarrow Li_6OSeI_2 + 4.8163\ CO_2$
	6	0.11	$4.0\ C + I_2O_5 + 2.0\ Li_2O_2 + Li_2Se \rightarrow Li_6OSeI_2 + 4.0\ CO_2$
	7	0.10	$Li_2Se + 2.0\ LiC_{12} + 2.0\ LiI + 24.5\ O_2 \rightarrow Li_6OSeI_2 + 24.0\ CO_2$
	13	0.10	$I_2O_5 + Li_2Se + 4.0\ LiC_{12} + 46.0\ O_2 \rightarrow Li_6OSeI_2 + 48.0\ CO_2$
Cmcm $Li_{12}O_3SeClBr_3$	3	0.10	$1.5\ Br_2O_3 + ClO_3 + 4.71\ Li_2O_2 + Li_2Se + 0.58\ LiC_{12} \rightarrow Li_{12}O_3SeClBr_3 + 6.96\ CO_2$ (Δ_{10})
	6	0.10	$1.5\ Br_2O_3 + Li_2Se + 9.0\ LiC_{12} + LiClO_4 + 105.25\ O_2 \rightarrow Li_{12}O_3SeClBr_3 + 108.0\ CO_2$ (Δ_{11})
	8	0.10	$1.5\ Br_2O_3 + 0.5\ Cl_2O_7 + Li_2Se + 10.0\ LiC_{12} + 117.5\ O_2 \rightarrow Li_{12}O_3SeClBr_3 + 120.0\ CO_2$

Discussion

The present multi-objective optimization task has successfully shortlisted over 10,000 *in-silico ip* compounds down to a few candidates for SE use. Instead of simply relying on recorded compounds from established structure databases, the target chemical space was largely extended through a systematic approach of generating derivative structures based on anion-site alloying and symmetry group-subgroup relations. This approach allows for potentially novel but often missed-out compounds to be uncovered in the SE screening procedure.

Out of the 3 SE-property objective functions, f_1: E_g is the least-costly to obtain as it can be readily derived with no extra computing cost after DFT geometry optimization. Since there is a systematic offset of the PBE-level E_g values relative to more accurate but more expensive calculation approaches (e.g., GW method),[81] a meaningful ranking of compounds is still achieved. Aside from *t-ip* structures, correlations are also successfully established for E_g, E_d, and $t_{G,ip}$ to include for *c-ip* structures as well, further confirming the general utility of $t_{G,ip}$ as a substitute parameter for E_g and E_d.

Based on f_2: E_h, most of screened *ip* compounds are predicted be reactive to moisture. This reactivity is consistent with the hard-soft acid-base theory, considering Li is a hard acid (in Li-rich *ip* compounds) and H_2O molecule is a hard base. It is noted that some of the compounds have $E_h > 0$, but their values are close to the endothermic-exothermic reaction crossover point ($E_h = 0$). This means that in the presence of other exothermic side reactions, proton incorporation is still conceivable for the said compounds. One likely reaction is related to LiOH (a possible secondary or pre-existing phase) and CO_2 (as a contaminant from air):

$$LiOH + \frac{1}{2}CO_2 \rightarrow \frac{1}{2}Li_2CO_3 + \frac{1}{2}H_2O. \qquad (33)$$

The calculated DFT reaction energy for equation (32) is -60.5 kJ/mol. With this additional heat source, all the screened compounds are predicted to likely react with H_2O under air-exposed condition. Experimental observations have demonstrated on the ease of protonation of some known *ip* compounds.[80-82]

Based on f_3: Λ, *Cmcm* $Li_{12}O_3SeClBr$ can be considered as the best compound (0.78 S/cm). It has a cubic Li_3XZ base structure with a continuous bcc-type anion X-Z_8 and Z-X_8 sublattices in 3 cell directions. This anion framework has been suggested previously to facilitate for a fast 3D diffusion pathway for Li^+ ions.[85] However, its composition complexity indicates a difficulty in actually synthesizing it in high phase purity because of competing phases that can likely form with it. Meanwhile, for *t-ip* compounds, the linkage of X-Z_8 and Z-X_8 bcc-type units are interrupted in the long-axis direction. As a result, fast ion conduction is constrained in 2D within each of the X-Z-Li slab layer units. This suggests a potential morphology-dependent conductivity in this structure type, such as if the exposed particle facet can facilitate for a fast inter-grain transport or not. Also, it is cautioned that although the bulk conductivities of the screened compounds are promising, they can have significantly different total conductivities, depending on the type of bulk defects present, the extent of proton incorporation, and the activation energy at the grain boundary region.[29, 82-84,86-89]

Several candidate synthesis routes are predicted for the screened *ip* compounds in the present work. For example, $Fm\overline{3}m$ Li_6OSeI_2 can be synthesized under typical solid state reaction conditions, without forming extra phases and with minimal nucleation barrier. Thus, this material may serve as a promising candidate for actual synthesis. Meanwhile, other candidate compounds are shown to have reactions that involve phase competition. This may reflect the general difficulty of stoichiometry control at elevated temperatures for *ip* compounds, since the typical reactants are highly susceptible to undergo sublimation (e.g., Li_2Se, Li_2S, LiCl, and LiBr).[90] Some synthesis routes are predicted to have no secondary phase formation, such as in the case of *I*4/*mmm* Li_4OBr_2, but it requires a high nucleation barrier for the reaction to proceed. An attempt to synthesize Li_4OBr_2 by high-pressure synthesis has been reported, but it resulted in a slightly different structure.[91]

Conclusions

Using high-throughput DFT and machine learning techniques, a large-scale material screening and evaluation was performed on a ten-thousand-scale *ip*-compound space, with a goal to find novel SEs that can satisfy multiple property criteria. Some of the key findings are as follows:

i) Out of 10,173 *in-silico* compounds, 1,413 compounds are found to have a high likelihood of synthesizability based on DFT-calculated thermodynamic decomposition energy (E_d) and experimental crystal-likeness score (L_s).

ii) The modified formulation of the Goldschmidt tolerance factor ($t_{G,ip}$) can serve as good descriptor for thermodynamic phase stability and E_g.

iii) There are 24 promising *ip* SEs that are determined by the present material screening methodology, examples include *Cm* $Li_8O_2Cl_3Br$ (E_d = 0, L_s > 0.5, E_g = 4.74 eV, E_h = -33.22 kJ/mol, Λ = 9.0 x 10^{-4} S/cm), *Amm*2 Li_8OSCl_4 (E_d = 0.070 eV/atom, L_s > 0.5, E_g = 4.14 eV, E_h = -40.70 kJ/mol, Λ = 9.2 x 10^{-2} S/cm), and *Cmcm* $Li_{12}O_3SeClBr_3$ (E_d = 0.097 eV/atom, L_s > 0.5, E_g = 3.36 eV, E_h = -86.88 kJ/mol, Λ = 7.8 x 10^{-1} S/cm).

iii) The bulk Li^+ ion conductivity of *t-ip* and *c-ip* compounds is strongly dependent on the type of stabilized defects, with the defects related to Li interstitials resulting to higher conductivity and lower diffusion barrier, as compared to defects that promote Li vacancies.

iv) The synthesis of *t-ip* and *c-ip* compounds are predicted to be accompanied with the formation of competing phases with low nucleation barriers.

Our comprehensive work provides useful insights into the design of *ip*-type SEs.

Acknowledgments

Authors are thankful for the support in part by JST through ALCA-SPRING grant number JPMJAL1301, and COI-NEXT grant number JPMJPF2016; by JSPS KAKENHI grant numbers JP19H05815 and JP21K14729; and by MEXT as Materials Processing Science project ("Materealize") grant number JPMXP0219207397, and "Program for Promoting Research on the Supercomputer Fugaku" grant number JPMXP1020200301. The calculations were performed on the supercomputers at NIMS (Numerical Materials Simulator) and the supercomputer Fugaku at the RIKEN through the HPCI System Research Project (project ID: hp210105). Crystal structures were visualized using the VESTA software.[92] The python library Matplotlib was used for making the plots.[93]

.

Supporting Information

Table on DFT-calculated electronic band gap energy values of known inorganic solid electrolytes; details on MSD slope fitting procedure; figure on DFT-geometry-optimized structure of *I*4/*mmm* Li_4OBr_2 antiperovskite compound with an added Li interstitial in one of the OLi_6 octahedral basal plane; table on summary list on region-1 compounds from Figure 9 of the main text; table on candidate solid state reactions based on a data-driven approach in Reference 80 of the main text for $Pm\bar{3}m$ Li_3OCl, $I4/mmm$ Li_4OBr_2, $P4/nmm$ $Li_8O_2Cl_3Br$, $I4/mmm$ $Li_7O_2FBr_2$, $Fm\bar{3}m$ Li_6OSeI_2, and $Cmcm$ $Li_{12}O_3SeClBr_3$ compounds.

References

1. Janek, J.; Zeier, W. G. A solid future for battery development. *Nat. Energy* **2016**, 1, 16141.

2. Takada, K. Progress in solid electrolytes toward realizing solid-state lithium batteries. *J. Power Sources* **2018**, 394, 74-85.

3. Manthiram, A.; Yu, X. W.; Wang, S. F. Lithium battery chemistries enabled by solid-state electrolytes. *Nat. Rev. Mater.* **2017**, 2, 16103.

4. Goodenough, J. B.; Park, K. S. The Li-ion rechargeable battery: a perspective. *J. Am. Chem. Soc.* **2013**, 135 (4), 1167-1176.

5. Ye, L.; Li, X. A dynamic stability design strategy for lithium metal solid state batteries. *Nature* **2021**, 593, 218-222.

6. Xu, Chao; Märker, K.; Lee, J.; Mahadevegowda, A.; Reeves, P. J.; Day, S. J.; Groh, M. F.; Emge, S. P.; Ducati, C.; Mehdi, B. L.; Tang, C. C.; Grey, C. P. Bulk fatigue induced by surface reconstruction in layered Ni-rich cathodes for Li-ion batteries. *Nat. Mater.* **2021**, 20, 84-92.

7. Xin, F.; Zhou, H.; Chen, X.; Zuba, M.; Chernova, N.; Zhou, G.; Whittingham, M. S., Li-Nb-O coating/substitution enhances the electrochemical performance of the $LiNi_{0.8}Mn_{0.1}Co_{0.1}O_2$ (NMC 811) cathode. *ACS Appl. Mater. Interfaces* **2019**, 11 (38), 34889-34894.

8. Lee, Y. G.; Fujiki, S.; Jung, C.; Suzuki, N.; Yashiro, N.; Omoda, R.; Ko, D. S.; Shiratsuchi, T.; Sugimoto, T.; Ryu, S.; Ku, J. H.; Watanabe, T.; Park, Y.; Aihara, Y.; Im, D.; Han, I. T. High-energy long-cycling all-solid-state lithium metal batteries enabled by silver-carbon composite anodes. *Nat. Energy* **2020**, 5 (4), 299-308.

9. Cheng, E. J.; Kimura, T.; Shoji, M.; Ueda, H.; Munakata, H.; Kanamura, K. Ceramic-Based Flexible Sheet Electrolyte for Li Batteries. *ACS Appl. Mater. Interfaces* **2020**, 12 (9), 10382-10388.

10. Kato, Y.; Hori, S.; Saito, T.; Suzuki, K.; Hirayama, M.; Mitsui, A.; Yonemura, M.; Iba, H.; Kanno, R. High-power all-solid-state batteries using sulfide superionic conductors. *Nat. Energy* **2016**, 1, 16030.

11. Ye, L.; Li, X. A dynamic stability design strategy for lithium metal solid state batteries. *Nature* **2021**, 593, 218-222.

12. Wang, M. J.; Carmona, E.; Gupta, A.; Albertus, P.; Sakamoto, J. Enabling "lithium-free" manufacturing of pure lithium metal solid-state batteries through in situ plating. *Nat. Commun.* **2020**, 11, 5201.

13. Samson, A. J.; Hofstetter, K.; Bag, S.; Thangadurai, V. A bird's-eye view of Li-stuffed garnet-type $Li_7La_3Zr_2O_{12}$ ceramic electrolytes for advanced all-solid-state Li batteries. *Energy Environ. Sci.* **2019**, 12 (10), 2957-2975.

14. Otoyama, M.; Sakuda, A.; Tatsumisago, M.; Hayashi, A. Sulfide Electrolyte Suppressing Side Reactions in Composite Positive Electrodes for All-Solid-State Lithium Batteries. *ACS Appl. Mater. Interfaces* **2020**, 12 (26), 29228-29234.

15. Yu, C. Y.; Choi, J.; Anandan, V.; Kim, J. H. High-Temperature Chemical Stability of $Li_{1.4}Al_{0.4}Ti_{1.6}(PO_4)_3$ Solid Electrolyte with Various Cathode Materials for Solid-State Batteries. *J. Phys Chem. C* **2020**, 124 (28), 14963-14971.

16. Zhang, Y.; He, X. F.; Chen, Z. Q.; Bai, Q.; Nolan, A. M.; Roberts, C. A.; Banerjee, D.; Matsunaga, T.; Mo, Y. F.; Ling, C. Unsupervised discovery of solid-state lithium ion conductors. *Nat. Commun.* **2019**, 10, 5260.

17. Harada, M.; Takeda, H.; Suzuki, S.; Nakano, K.; Tanibata, N.; Nakayama, M.; Karasuyama, M.; Takeuchi, I. Bayesian-optimization-guided experimental search of NASICON-type solid electrolytes for all-solid-state Li-ion batteries. *J. Mater. Chem. A* **2020**, 8 (30), 15103-15109.

18. Sendek, A. D.; Yang, Q.; Cubuk, E. D.; Duerloo, K. A. N.; Cui, Y.; Reed, E. J. Holistic computational structure screening of more than 12 000 candidates for solid lithium-ion conductor materials. *Energy Environ. Sci.* **2017**, 10 (1), 306-320.

19. Sendek, A. D.; Cubuk, E. D.; Antoniuk, E. R.; Cheon, G.; Cui, Y.; Reed, E. J. Machine Learning-Assisted Discovery of Solid Li-Ion Conducting Materials. *Chem. Mater.* **2019**, 31 (2), 342-352.

20. Cubuk, E. D.; Sendek, A. D.; Reed E. J. Screening billions of candidates for solid lithium-ion conductors: A transfer learning approach for small data. *J. Chem. Phys.* **2019**, 150 (21), 214701.

21. Zhu, Z. Y.; Chu, I. H.; Ong, S. P. $Li_3Y(PS_4)_2$ and $Li_5PS_4Cl_2$: New Lithium Superionic Conductors Predicted from Silver Thiophosphates using Efficiently Tiered Ab Initio Molecular Dynamics Simulations. *Chem. Mater.* **2017**, 29 (6), 2474-2484.

22. Ahmad, Z.; Xie, T.; Maheshwari, C.; Grossman, J. C.; Viswanathan, V. Machine Learning Enabled Computational Screening of Inorganic Solid Electrolytes for Suppression of Dendrite Formation in Lithium Metal Anodes. *ACS Central Sci.* **2018**, 4 (8), 996-1006.

23. Braga, M. H.; Ferreira, J. A.; Stockhausen, V.; Oliveira, J. E.; El-Azab, A. Novel Li_3ClO based glasses with superionic properties for lithium batteries. *J. Mater. Chem. A* **2014**, 2 (15), 5470-5480.

24. Zhao, Y. S.; Daemen, L. L. Superionic Conductivity in Lithium-Rich Anti-Perovskites. *J. Am. Chem. Soc.* **2012**, 134 (36), 15042-15047.

25. Li, Y. T.; Zhou, W. D.; Xin, S.; Li, S.; Zhu, J. L.; Lu, X. J.; Cui, Z. M.; Jia, Q. X.; Zhou, J. S.; Zhao, Y. S.; Goodenough, J. B. Fluorine-Doped Antiperovskite Electrolyte for All-Solid-State Lithium-Ion Batteries. *Angew. Chem. Int. Edit.* **2016**, 55 (34), 9965-9968.

26. Dawson, J. A.; Famprikis, T.; Johnston, K. E. Anti-perovskites for solid-state batteries: recent developments, current challenges and future prospects. *J. Mater. Chem. A* **2021**, 9 (35), 18746-18772.

27. Xia, W.; Zhao, Y.; Zhao, F.; Adair, K.; Zhao, R.; Li, S.; Zou, R.; Zhao, Y.; Sun X. Antiperovskite Electrolytes for Solid-State Batteries. *Chem. Rev.* **2022**, 122 (3), 3763-3819.

28. Glasser, L. Systematic Thermodynamics of Layered Perovskites: Ruddlesden-Popper Phases. *Inorg. Chem.* **2017**, 56 (15), 8920-8925.

29. Jalem, R.; Tateyama, Y.; Takada, K.; Nakayama, M. First-Principles DFT Study on Inverse Ruddlesden-Popper Tetragonal Compounds as Solid Electrolytes for All-Solid-State Li^+-Ion Batteries, *Chem. Mater.* **2021**, 33 (15), 5859-5871.

30. Kresse, G. Ab-Initio Molecular-Dynamics for Liquid-Metals. *J. Non-Cryst. Solids* **1995**, 193, 222-229.

31. Kresse, G.; Furthmuller, J. Efficient iterative schemes for ab initio total-energy calculations using a plane-wave basis set. *Phys. Rev. B* **1996**, 54 (16), 11169-11186.

32. Perdew, J. P.; Wang, Y. Accurate and Simple Analytic Representation of the Electron-Gas Correlation-Energy. *Phys. Rev. B* **1992**, 45 (23), 13244-13249.

33. Blochl, P. E. Projector Augmented-Wave Method. *Phys. Rev. B* **1994**, 50 (24), 17953-17979.

34. Kresse, G.; Joubert, D. From ultrasoft pseudopotentials to the projector augmented-wave method. *Phys. Rev. B* **1999**, 59 (3), 1758-1775.

35. Perdew, J. P.; Burke, K.; Ernzerhof, M. Generalized gradient approximation made simple. *Phys. Rev. Lett.* **1996**, 77 (18), 3865-3868.

36. Perdew, J. P.; Ruzsinszky, A.; Csonka, G. I.; Vydrov, O. A.; Scuseria, G. E.; Constantin, L. A.; Zhou, X. L.; Burke, K. Restoring the density-gradient expansion for exchange in solids and surfaces. *Phys. Rev. Lett.* **2008**, 100, 136406.

37. Bergerhoff, G. & Brown, I.D. in Crystallographic Databases, F.H. Allen et al. (Hrsg.) Chester, *International Union of Crystallography*, (**1987**).

38. Monkhorst, H. J.; Pack, J. D. Special Points for Brillouin-Zone Integrations. *Phys. Rev. B* **1976**, 13 (12), 5188-5192.

39. Ong, S. P.; Wang, L.; Kang, B.; Ceder, G. Li-Fe-P-O_2 phase diagram from first principles calculations. *Chem. Mater.* **2008**, 20 (5), 1798-1807.

40. Jain, A.; Ong, S. P.; Hautier, G.; Chen, W.; Richards, W. D.; Dacek, S.; Cholia, S.; Gunter, D.; Skinner, D.; Ceder, G.; Persson, K. A. Commentary: The Materials Project: A materials genome approach to accelerating materials innovation. *APL Mater.* **2013**, 1, 011002.

41. Ong, S. P.; Richards, W. D.; Jain, A.; Hautier, G.; Kocher, M.; Cholia, S.; Gunter, D.; Chevrier, V. L.; Persson, K. A.; Ceder, G. Python Materials Genomics (pymatgen): A robust, open-source python library for materials analysis. *Comp. Mater. Sci.* **2013**, 68, 314-319.

42. Binninger, T.; Marcolongo, A.; Mottet, M.; Weber, V.; Laino, T. Comparison of computational methods for the electrochemical stability window of solid-state electrolyte materials. *J. Mater. Chem. A* **2020**, 8 (3), 1347-1359.

43. Hanghofer, I.; Redhammer, G. J.; Rohde, S.; Hanzu, I.; Senyshyn, A.; Wilkening, H. M. R.; Rettenwander, D. Untangling the Structure and Dynamics of Lithium-Rich Anti-Perovskites Envisaged as Solid Electrolytes for Batteries. *Chem. Mater.* **2018**, 30 (22), 8134-8144.

44. Chen, H. M.; Chen, M. H.; Adams, S. Stability and ionic mobility in argyrodite-related lithium-ion solid electrolytes. *Phys. Chem. Chem. Phys.* **2015**, 17 (25), 16494-16506.

45. Persson, K. A.; Waldwick, B.; Lazic, P.; Ceder, G. Prediction of solid-aqueous equilibria: Scheme to combine first-principles calculations of solids with experimental aqueous states. *Phys. Rev. B - Condens. Matter Mater. Phys.* **2012**, 85 (23), 235438.

46. Kubaschewskii, O.; Alcock, C. B.; Spencer, P. J. Materials Thermochemistry, 6th ed.; *Pergamon, New York*: **1992**.

47. Emly, A.; Kioupakis, E.; Van der Ven, A. Phase Stability and Transport Mechanisms in Antiperovskite Li_3OCl and Li_3OBr Superionic Conductors. *Chem. Mater.* **2013**, 25 (23), 4663-4670.

48. Hoover, W. G.; Ladd, A. J. C.; Moran, B. High-Strain-Rate Plastic-Flow Studied Via Non-Equilibrium Molecular-Dynamics. *Phys. Rev. Lett.* **1982**, 48 (26), 1818-1820.

49. Nose, S. A Unified Formulation of the Constant Temperature Molecular-Dynamics Methods. *J. Chem. Phys.* **1984**, 81 (1), 511-519.

50. He, Y.; Burov, S.; Metzler, R.; Barkai, E. Random time-scale invariant diffusion and transport coefficients. *Phys. Rev. Lett.* **2008**, 101, 058101.

51. Atkins, P., Atkins' Physical Chemistry. 11 ed.; *Oxford University Press*: **2006**; p 1040.

52. Nitzan, A. Chemical Dynamics in Condensed Phases: Relaxation, Transfer and Reactions in Condensed Molecular Systems. Oxford Graduate Texts; *Oxford University Press: Oxford*: **2006**.

53. Jalem, R.; Nakayama, M.; Noda, Y.; Le, T.; Takeuchi, I.; Tateyama, Y.; Yamazaki, H. A general representation scheme for crystalline solids based on Voronoi-tessellation real feature values and atomic property data. *Sci. Technol. Adv. Mat.* **2018**, 19 (1), 231-242.

54. Feliot, P.; Bect, J.; Vazquez, E. A Bayesian approach to constrained single- and multi-objective optimization. *J. Global Optim.* **2017**, 67 (1-2), 97-133.

55. Rasmussen, C. E.; Williams, C. K. I. Gaussian Processes for Machine Learning (Adaptive Computation and Machine Learning series), *the MIT Press* **2005**, 1-247.

56. Mackay, D. J. C. Information Theory, Inference, and Learning Algorithms. *Cambridge University Press: UK* **2003**.

57. Jones, D. R. A taxonomy of global optimization methods based on response surfaces. *J. Global Optim.* **2001**, 21 (4), 345-383.

58. Jalem, R.; Kanamori, K.; Takeuchi, I.; Nakayama, M.; Yamasaki, H.; Saito, T. Bayesian-Driven First-Principles Calculations for Accelerating Exploration of Fast Ion Conductors for Rechargeable Battery Application. *Sci. Rep.* **2018**, 8, 5845.

59. Scholkopf, B.; Smola, A.; Muller, K. R. Nonlinear component analysis as a kernel eigenvalue problem. *Neural Comput.* **1998**, 10 (5), 1299-1319.

60. Pedregosa, F.; Varoquaux, G.; Gramfort, A.; Michel, V.; Thirion, B.; Grisel, O.; Blondel, M.; Prettenhofer, P.; Weiss, R.; Dubourg, V.; Vanderplas, J.; Passos, A.; Cournapeau, D.; Brucher, M.; Perrot,

M.; Duchesnay, E. Scikit-learn: Machine Learning in Python. *J. Mach. Learn. Res.* **2011**, 12 (85), 2825-2830.

61. GPy. GPy: A Gaussian process framework in python. *http://github.com/SheffieldML/GPy* (**2012**).

62. Biscani, F. I.; Izzo, D. A parallel global multiobjective framework for optimization: pagmo. *J. Open Source Softw.* **2020**, 5 (53), 2338.

63. Hart, G. L. W.; Forcade, R. W. Algorithm for generating derivative structures. *Phys. Rev. B* **2008**, 77 (22).

64. Banik, A.; Famprikis, T.; Ghidiu, M.; Ohno, S.; Kraft, M. A.; Zeier, W. G. On the underestimated influence of synthetic conditions in solid ionic conductors. *Chem. Sci.* **2021**, 12 (18), 6238-6263.

65. Sun, W. H.; Dacek, S. T.; Ong, S. P.; Hautier, G.; Jain, A.; Richards, W. D.; Gamst, A. C.; Persson, K. A.; Ceder, G. The thermodynamic scale of inorganic crystalline metastability. *Sci. Adv.* **2016**, 2 (11), e1600225.

66. Goldschmidt, V. M. Die Gesetze der Krystallochemie. *Naturwissenschaften* **1926**, 14, 477-485.

67. Wang, Z.; Xu, H.; Xuana, M.; Shao, G. From anti-perovskite to double anti-perovskite: tuning lattice chemistry to achieve super-fast Li^+ transport in cubic solid lithium halogen-chalcogenides. *J. Mater. Chem. A* **2018**, 6 (1), 73-83.

68. Zhu, Y.; He, X.; Mo, Y. First principles study on electrochemical and chemical stability of solid electrolyte-electrode interfaces in all-solid-state Li-ion batteries. *J. Mater. Chem. A* **2016**, 4, 3253-3266.

69. Fujita, Y.; Hakari, T.; Sakuda, A.; Deguchi, M.; Kawasaki, Y.; Tsukasaki, H.; Mori, S.; Tatsumisago, M.; Hayashi, A. Li_2S-LiI Solid Solutions with Ionic Conductive Domains for Enhanced All-Solid-State Li/S Batteries. *ACS Appl. Energy Mater.* **2022**, 5 (8), 9429-9436.

70. Ma, X.; Xu, Y. Enhanced critical current density of Garnet $Li_7La_3Zr_2O_{12}$ solid electrolyte by incorporation of LiBr. *Electrochim. Acta* **2022**, 409, 139986.

71. Kikuchi, H.; Iyetomi, H.; Hasegawa, A. Insight into the origin of superionic conductivity from electronic structure theory. *J. Phys.: Condens. Matter* **1998**, 10, 11439-11448.

72. Lin, Z.; Liu, Z.; Dudney, N. J.; Liang, C. Lithium Superionic Sulfide Cathode for All-Solid Lithium-Sulfur Batteries. *ACS Nano* **2013**, 7 (3), 2829-2833.

73. Banerjee, A.; Wang, X.; Fang, C.; Wu, E. A.; Meng, Y. S. Interfaces and Interphases in All-Solid-State Batteries with Inorganic Solid Electrolytes. *Chem. Rev.* **2020**, 120 (14), 6878-6933.

74. Gao, B.; Jalem, R.; Ma, Y.; Tateyama, Y. Li^+ Transport Mechanism at the Heterogeneous Cathode/Solid Electrolyte Interface in an All-Solid-State Battery via the First-Principles Structure Prediction Scheme. *Chem. Mater.* **2020**, 32 (1), 85-96.

75. Komatsu, H.; Banerjee, S.; Chandrappa, M. L. H.; Qi, J.; Radhakrishnan, B.; Kuwata, S.; Sakamoto, K.; Ong, S. P. Interfacial Stability of Layered $LiNi_xMn_yCo_{1-x-y}O_2$ Cathodes with Sulfide Solid Electrolytes in All-Solid-State Rechargeable Lithium-Ion Batteries from First-Principles Calculations. *J. Phys. Chem. C* **2022**, 126 (41), 17482-17489.

76. Jalem, R.; Yamamoto, Y.; Shiiba, H.; Nakayama, M.; Munakata, H.; Kasuga, T.; Kanamura, K. Concerted Migration Mechanism in the Li Ion Dynamics of Garnet-Type $Li_7La_3Zr_2O_{12}$. *Chem. Mater.* **2013**, 25 (3), 425-430.

77. Morgan B. J., Lattice-geometry effects in garnet solid electrolytes: a lattice-gas Monte Carlo simulation study, *R. Soc. Open Sci.* **2017**, 4, 170824.

78. Yin, L.; Yuan, H.; Kong, L.; Lu, Z.; Zhao, Y. Engineering Frenkel defects of anti-perovskite solid-state electrolytes and their applications in all-solid-state lithium-ion batteries. *Chem. Commun.* **2020**, 56 (8), 1251-1254.

79. Jang, J.; Gu, G. H.; Noh, J.; Kim, J.; Jung, Y., Structure-Based Synthesizability Prediction of Crystals Using Partially Supervised Learning. *J. Am. Chem. Soc.* **2020**, 142 (44), 18836-18843.

80. Aykol, M.; Montoya, J. H.; Hummelshøj, J. Rational Solid-State Synthesis Routes for Inorganic Materials. *J. Am. Chem. Soc.* **2021**, 143 (24), 9244-9259.

81. Morales-García, Á.; Valero, R.; Illas, F. An Empirical, yet Practical Way To Predict the Band Gap in Solids by Using Density Functional Band Structure Calculations. *J. Phys. Chem. C* **2017**, 121 (34), 18862-18866.

82. Li, Y.; Zhou, W.; Xin, S.; Li, S.; Zhu, J.; Lü, X.; Cui, Z.; Jia, Q.; Zhou, J.; Zhao, Y.; Goodenough, J. B. Fluorine-Doped Antiperovskite Electrolyte for All-Solid-State Lithium-Ion Batteries. *Angew. Chem. Int. Ed.* **2016**, 55 (34), 9965-9968.

83. Sugumar, M. K.; Yamamoto, T.; Ikeda, K.; Motoyama, M.; Iriyama, Y. Preparation of Li-Excess and Li-Deficient Antiperovskite Structured $Li_{2+x}OH_{1-x}Br$ and Their Effects on Total Ionic Conductivity. *Inorg. Chem.* **2022**, 61 (11), 4655-4659.

84. Hanghofer, I.; Redhammer, G. J.; Rohde, S.; Hanzu, I.; Senyshyn, A.; Wilkening, H. M. R.; Rettenwander, D. Untangling the Structure and Dynamics of Lithium-Rich Anti-Perovskites Envisaged as Solid Electrolytes for Batteries. *Chem. Mater.* **2018**, 30 (22), 8134-8144.

85. Wang, Y.; Richards, W. D.; Ong, S. P.; Miara, L. J.; Kim, J. C.; Mo, Y.; Ceder, G. Design principles for solid-state lithium superionic conductors. *Nature Mater.* **2015**, 14, 1026-1031.

86. Zhang, Y.; Zhao, Y.; Chen, C. *Ab initio* study of the stabilities of and mechanism of superionic transport in lithium-rich antiperovskites. *Phys. Rev. B* **2013**, 87 (13), 134303.

87. Lu, Z.; Chen, C.; Baiyee, Z. M.; Chen, X.; Niu, C.; Ciucci, F. Defect chemistry and lithium transport in Li_3OCl anti-perovskite superionic conductors. *Phys. Chem. Chem. Phys.* **2015**, 17 (48), 32547-32555.

88. Dawson, J. A.; Attari, T. S.; Chen, H.; Emge, S. P.; Johnston, K. E.; Islam, M. S. Elucidating lithium-ion and proton dynamics in anti-perovskite solid electrolytes. *Energy Environ. Sci.* **2018**, 11 (10), 2993-3002.

89. Dawson, J. A.; Canepa, P.; Famprikis, T.; Masquelier, C.; Islam, M. S. Atomic-Scale Influence of Grain Boundaries on Li-Ion Conduction in Solid Electrolytes for All-Solid-State Batteries. *J. Am. Chem. Soc.* **2018**, 140 (1), 362-368.

90. Abudurusuli, A.; Wu, K.; Li, J. J.; Yalikun, A.; Yang, Z. H.; Pan, S. L. $LiBa_2M^{III}Q_4$ (M^{III} = Al, Ga, In; Q = S, Se): A Series of Metal Chalcogenides with a Structural Transition. *Inorg. Chem.* **2019**, 58 (19), 12859-12866.

91. Wakazaki, S.; Liu, Q.; Jalem, R.; Nishikubo, T.; Sakai, Y.; Matsui, N.; Zhao, G.; Suzuki, K.; Shigematsu, K.; Yamamoto, T.; Kanno, R.; Das, H.; Tateyama, Y.; Azuma, M. High-Pressure Synthesis and Lithium-Ion Conduction of Li_4OBr_2 Derivatives with a Layered Inverse-Perovskite Structure. *Chem. Mater.* **2021**, 33 (23) 9194-9201.

92. Momma, K.; Izumi, F., VESTA: A Three-Dimensional Visualization System for Electronic and Structural Analysis. *J. Appl. Crystallogr.* **2008**, 41 (3), 653-658.

93. Hunter, J. D. Matplotlib: A 2D Graphics Environment. *Comput. Sci. Eng.* **2007**, 9 (3), 90-95.

TABLE OF CONTENTS GRAPHIC